bone union at time 0. The rhFGF-2 dose dependently increased the percentage of patients with radiographic bone union during the observation period up to 16 weeks ($p = 0.015$ between the high and low dosage groups; $p = 0.035$ among the three groups) (Fig. 1A). The percentages of patients with radiographic bone union in the high dosage group was about three times and twice those in the low dosage group at 8 and 10 weeks, respectively. At 12 weeks and thereafter, even the low dosage group showed radiographic bone union, and eventually at 16 weeks all patients achieved radiographic bone union. All patients with bone union at earlier time points were confirmed to conserve the status until the last visit at 16 weeks without refracture. The times needed for 50% of patients in the low, middle, and high dosage groups to show radiographic bone union were 11.5, 10.1, and 8.1 weeks, respectively (Fig. 1A). In the meantime, the average times needed for radiographic bone union in the three groups were 11.5, 9.3, and 9.0 weeks, respectively (Fig. 1B). Figure 2 shows the time course of X-ray pictures of representative patients in the three groups. In the patients of the low dosage group, the bony bridging across the osteotomy gap was not apparent even at 10 weeks. In patients of middle and high dosage groups, on the contrary, the calcified callus was observed at 6 weeks and the bony bridging at 8 weeks following the surgery.

Clinical Outcomes

We next examined the effects of rhFGF-2 on clinical outcomes. The percentages of patients who were pain free at the osteotomy site, those with full-weight bearing on the operated leg, and those with clinical healing (defined as both radiographic bone union and pain free) were higher in middle- and high-dosage groups than in the low-dosage group, especially in the clinically critical periods 6, 8, and 10 weeks after the surgery (Fig. 3). However, at 12 weeks and thereafter, even the low-dosage group showed comparable clinical outcomes to the higher groups, just like radiographic bone union. All patients deemed clinically healed at earlier time points were confirmed to have conserved that status until the last visit without recurring pain or fracture.

Blood Chemistries

The serum calcium, phosphate, calcitonin, and osteocalcin levels were measured preoperatively, and 2 and 4 weeks postoperatively. No significant

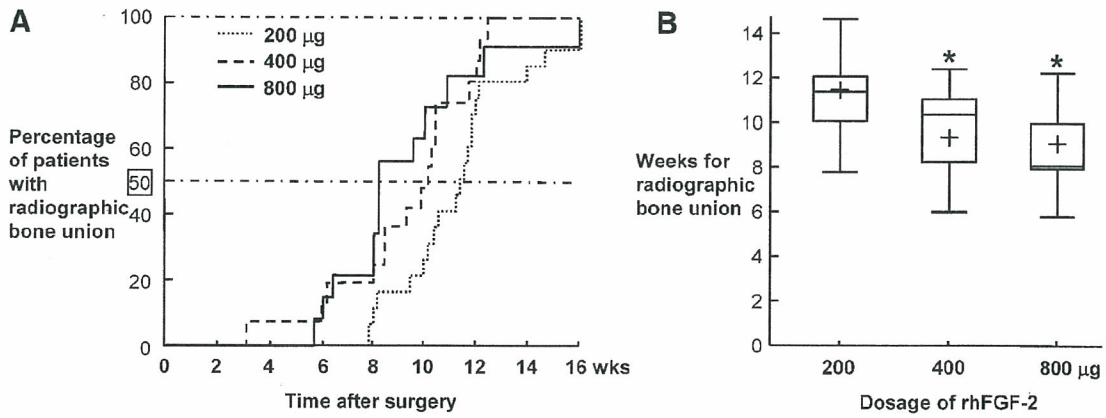

Figure 1. Comparison of radiographic bone union among patients with 200, 400, and 800 μg rhFGF-2 application. Radiographic bone union was defined as the apparent bridging by bony beam across the osteotomy gap on standard X-ray pictures that were taken immediately after the surgery and at least every 2 weeks threafter up to 16 weeks. (A) Time course of the percentage of patients with radiographic bone union during 16 weeks after the surgery in the three dosage groups. rhFGF-2 dose dependently increased the percentage of those with radiographic bone union ($p = 0.035$ among the three groups, and $p = 0.015$ between the high and low dosage groups). (B) Box and whisker plot representing weeks needed for radiographic bone union in the three dosage groups. The line through the box is the median; the top and bottom edges of each box represent the 25 and 75 percentiles, giving the interquartile range; and cross in the box is the mean. The vertical lines at each side of the box represent distribution from the quartiles to the farthest observation. *$p < 0.05$; significant difference from the 200 μg group by the Tukey-Kramer test.

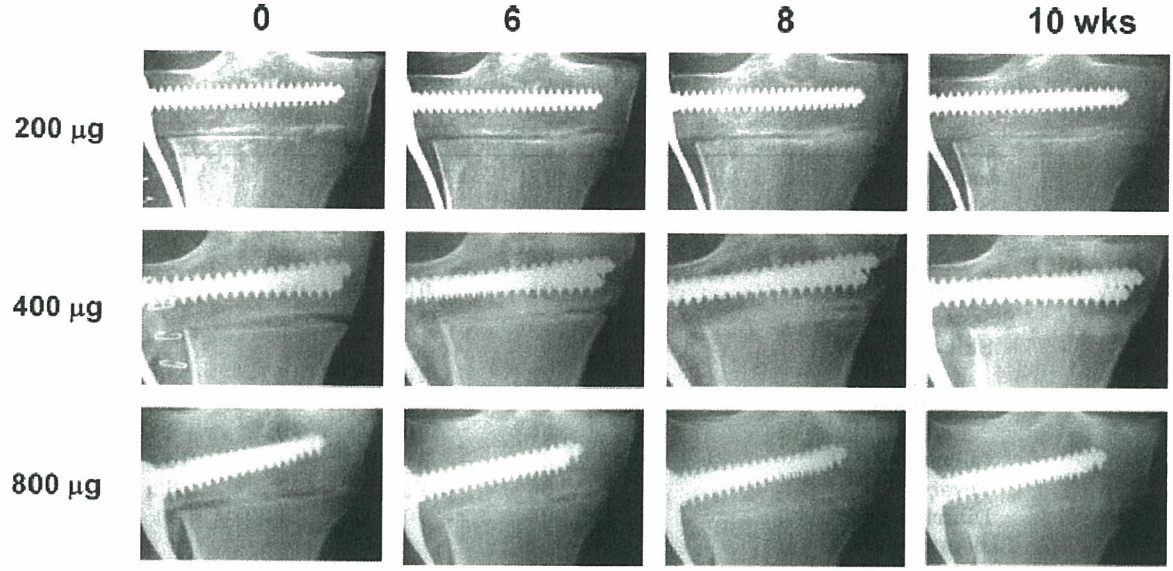

Figure 2. Anteroposterior X-ray pictures of tibial osteotomy sites of representative patients in the three dosage groups at 0, 6, 8, and 10 weeks after the surgery.

difference was detected in the calcium, phosphate, or osteocalcin levels among the three dosage groups, nor among the time points before and after the surgery (all $p > 0.05$). Although only the preoperative calcitonin level was higher in the low- dosage group, the levels became comparable after the surgery. The serum FGF-2 level also was not significantly affected by the dosage of applied rhFGF-2 at least up to 2 weeks after the application (all $p > 0.05$). Neither antibody to FGF-2 nor that to gelatin was detected in any patients preoperatively or postoperatively.

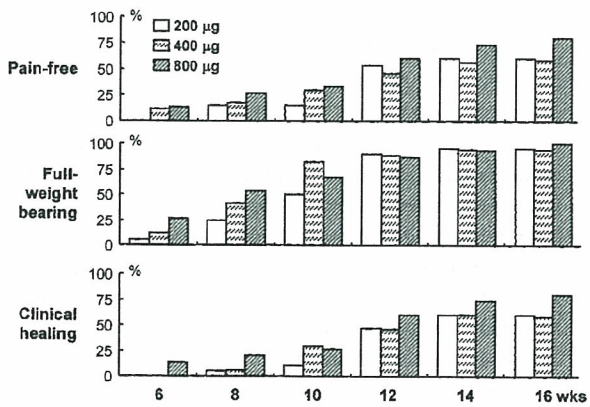

Figure 3. Comparison of clinical outcomes among patients with 200, 400, and 800 μg rhFGF-2 application. Cumulative percentage of patients with absence of pain at the osteotomy site, those with full weight bearing on the operated leg, and those with clinical healing (defined as both radiographic bone union and absence of pain) were compared every 2 weeks for 16 weeks after the surgery. The missing data of only one patient in the 400 μg group at 6 weeks were carried forward from those at 4 weeks.

Safety

The local or systemic adverse events experienced by the patients during the observation periods included several kinds of skin disorders, peroneal palsy, coryza, fever, and diarrhea (Table 2). Of the local skin disorders, the pin-site infection was most frequent and lasted 7–49 days. The durations of other systemic or local skin disorders such as eczema, eruption, and edema ranged 1–52 days. Two cases of peroneal palsy that were seen in the operated leg of the low dosage group lasted 28 and 105 days after surgery, and recovered within the obsevation period. Other systemic disorders: coryza, fever, and diarrhea were also temporary, and lasted 1–33 days. All the symptoms were classified as nonserious according to ICH Guidelines. Although the knee range of motion was not evaluated, there was no report of the disability as an adverse event. There was no case with hardware failure of the fixation device nor with heterotopic ossification of ligaments, tendons, or cartilage on X-ray during the obsevation periods. Regarding laboratory data, increases in the serum levels of C-reactive protein and fibrinogen levels may be due to the pin-infection, because both decreased to normal levels with disappearance of the infection. Slight increases in the glutamate–pyruvate–transaminase and eosinophil levels

DOI 10.1002/jor

Table 2. Adverse Events

	rhFGF-2			
	200 μg	400 μg	800 μg	Total
Local events				
Skin disorders				
Pin site infection	4	2	1	7
Eczema	0	0	1	1
Peroneal palsy	2	0	0	2
Systemic events				
Skin disorders				
Eczema	2	3	3	8
Eruption	1	1	2	4
Edema	0	0	3	3
Coryza	3	3	4	10
Fever	0	1	2	3
Diarrhea	0	0	1	1
Laboratory data				
C-reactive protein increase	2	0	1	3
Fibrinogen increase	0	0	1	1
Glutamate-pyruvate-transaminase increase	1	0	0	1
Eosinophil increase	1	0	0	1

were detected within 4 weeks after the surgery, and decreased to normal levels thereafter. All of these symptoms and abnormal laboratory data had recovered before the last visit at 16 weeks, and neither the number nor the duration statistically showed positive association with the dosages of the rhFGF-2 applied.

DISCUSSION

Based on the evidence of extensive studies using various animal models,[6–15] this study for the first time showed clinical evidence that rhFGF-2 in gelatin hydrogel accelerated radiographic bone union of the closing wedge high tibial osteotomy. Because most osteotomies can heal only with appropriate fixations, and in fact, all patients even of the low dosage group eventually achieved radiographic bone union in the present study, the rhFGF-2 application may not have yielded bone union by preventing nonunion, but just accelerated bone union. However, if the osteotomy site remains unstable for a long time, the chances of mal-union and infection causing skeletal deformity, late nerve palsy and refracture may increase. The reduction of time for bone union by the rhFGF-2 application is therefore important not only for the comfort of the patient after surgery, but also for the prevention of these secondary disorders.

FGF-2 is reported to stimulate the proliferation of immature mesenchymal cells but to inhibit the differentiation and matrix synthesis of osteoblastic cells.[18–22] Our preliminary experiments using the rat and rabbit models demonstrated that the local half-life of the injected ^{125}I-labeled FGF-2 in the gelatin hydrogel was 1 to 2 days. The percentages of the ^{125}I-labeled FGF-2 remaining localized were approximately 20, 3, and 1% at 1, 2, and 3 weeks, respectively. Hence, FGF-2 appears to have its effect primarily in the earlier stage of bone repair, probably through its mitogenic action on immature mesenchymal cells. In fact, previous animal studies demonstrated that a single injection of FGF-2 enhanced the proliferation of chondroprogenitor cells in fracture callus, causing the formation of a larger cartilage, but did not directly affect maturation of chondrocytes or replacement of the cartilage by osseous tissue.[7,14,23] Furthermore, expressions of FGF-2, FGF-1, and their principal receptor FGFR1 have been identified mainly at the early stage of fracture healing.[1,24–26] In addition to its mitogenic action on immature mesenchymal cells, FGF-2 may induce other anabolic factors such as prostaglandins, transforming growth factor (TGF)-β and bone morphogenetic proteins (BMPs), which may compose a serial cascade of bone formation. In fact, we and others have shown that FGF-2 induces TGF-β expression and prostaglandin production in a rat fracture model and in cultured osteoblastic cells.[7,27,28] Because the present blood chemistries indicate the absence of influence on systemic bone turnover and metabolism, FGF-2 may act as a local

factor that initiates the cascade of bone formation in the entire bone repair process. The follow-up period for 16 weeks might be relatively short for the safety conclusions. However, considering the above pharmacokinetics of rhFGF-2 in the gelatin hydrogel, we assume that the effect may possibly not persist after 16 weeks.

Among growth factors that have been investigated to date, BMPs appear to be the most popular that exhibit a potent osteoanabolic activity. Unlike FGF-2, BMPs strongly stimulate the differentiation and matrix synthesis of osteoprogenitor cells.[29,30] Regarding the clinical applications, three randomized trials have led to various regulatory agency approvals for specific indications of rhBMPs in the United States and other countries.[31–33] Two of them showed the positive effects on bone repair: one for rhBMP-2 on open tibial fractures[32] and the other for rhBMP-7 (rhOP-1) on tibial nonunions.[33] However, considering that as much as 12 mg of rhBMP-2 and 3.5 mg of rhBMP-7 were needed to show positive effects in those studies, bone anabolic potencies of the BMPs in clinical settings are not as impressive as those seen in animal models in which more robust bone formation and healing have been observed.[29,30] This may be because BMPs may be degraded more quickly in humans than in animals, the biology of the receptor–ligand interactions may differ, or the pharmacokinetics of the activity may be less favorable in humans.

The most important limitation of the present study is the lack of the vehicle control group (the gelatin hydrogel only). IRB of several institutions did not deem it ethically acceptable because systemic immediate-type reactions, including anaphylactic shock, to measles, mumps, rubella, and varicella vaccines reported in some children were suspected to be allergic symptoms caused by gelatin antigen that is included in the vaccines as a stabilizer.[34] The present gelatin hydrogel was therefore originally synthesized by deleting the antigenic portion.[16,17] We believe that the present result showing the absence of the antibody in the patients may lead to the approval of the clinical use of the gelatin hydrogel as the rhFGF-2 carrier. Instead of the control group, we determined the three dosages of rhFGF-2 based on previous preclinical results of osteotomy experiments on animals.[7–9,12] When the dosages in the animal studies were converted to the area of the human proximal tibiae, 800 μg of rhFGF-2 was expected to show a significant anabolic function, while 200 μg exerted little effect. In fact, the high dosage of rhFGF-2 showed significant bone anabolic function over the low dosage in the present clinical study. Furthermore, all patients of the low-dosage group also eventually achieved bone union after 16 weeks, although a previous report on the natural course of high tibial osteotomy showed that 8.5 and 5.7% remained nonunion even after 6 months and 1 year, respectively.[35] Hence, unlike BMPs, the discrepancy of bone anabolic potency between animals and humans may not be seen in the function of FGF-2. However, because the rationale for the present dose selection was not based on prior clinical evaluations to determine the dose with maximum efficacy, we are now planning a clinical trial using higher amounts of rhFGF-2.

In conclusion, the present dose–escalation clinical trial revealed that rhFGF-2 in gelatin hydrogel dose dependently accelerated bone repair of the tibial osteotomy with a safety profile. Because the formulation of the rhFGF-2 gelatin hydrogel is slightly viscid, it not only can be applied to the osteotomy site during the surgical procedure, but also can be percutaneously injected under roentgenologic guidance at the time of closed reduction of a bone fracture followed by a fixation with casting. We are now planning a more advanced clinical trial on fresh tibial fractures including a control group for the application of regulatory agency approval to obtain clinical indication of this agent. Furthermore, the development of appropriate delivery systems may yield progress; for example, a sequential delivering system of FGF-2 at the earlier stage and other differentiation factors like BMPs at the later stage might have potential as the optimal method of inducing bone formation. The extensive application of the osteoanabolic nature of FGF-2 to various skeletal disorders will be explored in the near future.

ACKNOWLEDGMENTS

This work was supported by Grants-in-Aid for Scientific Research from the Japanese Ministry of Education, Culture, Sports, Science and Technology, which had no role in study design, data collection, data analysis, data interpretation, or writing of the report. We declare that we have no conflict of interest.

REFERENCES

1. Lieberman JR, Daluiski A, Einhorn TA. 2002. The role of growth factors in the repair of bone biology and clinical applications. J Bone Joint Surg [Am] 84:1032–1044.
2. Itoh N, Ornitz DM. 2004. Evolution of the Fgf and Fgfr gene families. Trends Genet 20:563–569.
3. Canalis E, Centrella M, McCarthy T. 1988. Effects of basic fibroblast growth factor on bone formation in vitro. J Clin Invest 81:1572–1577.

DOI 10.1002/jor

4. Khan SN, Bostrom MP, Lane JM. 2000. Bone growth factors. Orthop Clin North Am 31:375–388.
5. Coumoul X, Deng CX. 2003. Roles of FGF receptors in mammalian development and congenital diseases. Birth Defects Res C Embryo Today 69:286–304.
6. Aspenberg P, Lohmander LS. 1989. Fibroblast growth factor stimulates bone formation. Acta Orthop Scand 60: 473–476.
7. Kawaguchi H, Kurokawa T, Hanada K, et al. 1994. Stimulation of fracture repair by recombinant human basic fibroblast growth factor in normal and streptozotocin-diabetic rats. Endocrinology 135:774–781.
8. Kato T, Kawaguchi H, Hanada K, et al. 1998. Single local injection of recombinant fibroblast growth factor-2 stimulates healing of segmental bone defects in rabbits. J Orthop Res 16:654–659.
9. Nakamura T, Hara Y, Tagawa M, et al. 1998. Recombinant human basic fibroblast growth factor accelerates fracture healing by enhancing callus remodeling in experimental dog tibial fracture. J Bone Miner Res 13:942–949.
10. Radomsky ML, Aufdemorte TB, Swain LD, et al. 1999. Novel formulation of fibroblast growth factor-2 in a hyaluronan gel accelerates fracture healing in nonhuman primates. J Orthop Res 17:607–614.
11. Tabata Y, Yamada K, Hong L, et al. 1999. Skull bone regeneration in primates in response to basic fibroblast growth factor. J Neurosurg 91:851–856.
12. Kawaguchi H, Nakamura K, Tabata Y, et al. 2001. Acceleration of fracture healing in non-human primates by fibroblast growth factor-2. J Clin Endocrinol Metab 86:875–880.
13. Okazaki H, Kurokawa T, Nakamura K, et al. 1999. Stimulation of bone formation by recombinant fibroblast growth factor-2 in callotasis bone lengthening of rabbits. Calcif Tissue Int 64:542–546.
14. Nakamura K, Kawaguchi H, Aoyama I, et al. 1997. Stimulation of bone formation by intraosseous application of recombinant basic fibroblast growth factor in normal and ovariectomized rabbits. J Orthop Res 15:307–313.
15. Nakamura T, Hanada K, Tamura M, et al. 1995. Stimulation of endosteal bone formation by systemic injections of recombinant basic fibroblast growth factor in rats. Endocrinology 136:1276–1284.
16. Tabata Y, Ikada Y. 1999. Vascularization effect of basic fibroblast growth factor released from gelatin hydrogels with different biodegradabilities. Biomaterials 20:2169–2175.
17. Tabata Y, Nagano A, Ikada Y. 1999. Biodegradation of hydrogel carrier incorporating fibroblast growth factor. Tissue Eng 5:127–138.
18. Hurley MM, Abreu C, Harrison JR, et al. 1993. Basic fibroblast growth factor inhibits type I collagen gene expression in osteoblastic MC3T3-E1 cells. J Biol Chem 268:5588–5593.
19. Hurley MM, Kessler M, Gronowicz G, et al. 1992. The interaction of heparin and basic fibroblast growth factor on collagen synthesis in 21-day fetal rat calvariae. Endocrinology 130:2675–2682.
20. Kato Y, Iwamoto M. 1990. Fibroblast growth factor is an inhibitor of chondrocyte terminal differentiation. J Biol Chem 265:5903–5909.
21. McCarthy TL, Centrella M, Canalis E. 1989. Effects of fibroblast growth factors on deoxyribonucleic acid and collagen synthesis in rat parietal bone cells. Endocrinology 125:2118–2126.
22. Rodan SB, Wesolowski G, Kyonggeun Y, Rodan GA. 1989. Opposing effects of fibroblast growth factor and pertussis toxin on alkaline phosphatase, osteopontin, osteocalcin and type I collagen mRNA levels in ROS 17/2.8 cells. J Biol Chem 264:19934–19941.
23. Nakajima F, Ogasawara A, Goto K, et al. 2001. Spatial and temporal gene expression in chondrogenesis during fracture healing and the effects of basic fibroblast growth factor. J Orthop Res 19:935–944.
24. Bolander ME. 1992. Regulation of fracture repair by growth factors. Proc Soc Exp Biol Med 200:165–170.
25. Bourque WT, Gross M, Hall BK. 1993. Expression of four growth factors during fracture repair. Int J Dev Biol 37: 573–579.
26. Nakajima A, Nakajima F, Shimizu S, et al. 2001. Spatial and temporal gene expression for fibroblast growth factor type I receptor (FGFR1) during fracture healing in the rat. Bone 29:458–466.
27. Kawaguchi H, Pilbeam CC, Gronowicz G, et al. 1995. Transcriptional induction of prostaglandin G/H synthase-2 by basic fibroblast growth factor. J Clin Invest 96:923–930.
28. Noda M, Vogel R. 1989. Fibroblast growth factor enhances type β1 transforming growth factor gene expression in osteoblast-like cells. J Cell Biol 109:2529–2535.
29. Einhorn TA. 2003. Clinical applications of recombinant human BMPs: early experience and future development. J Bone Joint Surg [Am] 85:82–88.
30. Luppen CA, Blake CA, Ammirati KM, et al. 2002. Recombinant human bone morphogenetic protein-2 enhances osteotomy healing in glucocorticoid-treated rabbits. J Bone Miner Res 17:301–310.
31. Burkus JK, Gornet MF, Dickman CA, et al. 2002. Anterior lumbar interbody fusion using rhBMP-2 with tapered interbody cages. J Spinal Disord Tech 15:337–349.
32. Govender S, Csimma C, Genant HK, et al. 2002. Recombinant human bone morphogenetic protein-2 for treatment of open tibial fractures: a prospective, controlled, randomized study of four hundred and fifty patients. J Bone Joint Surg [Am] 84:2123–2134.
33. Friedlaender GE, Perry CR, Cole JD, et al. 2001. Osteogenic protein-1 (bone morphogenetic protein-7) in the treatment of tibial nonunions. J Bone Joint Surg [Am] 83(Suppl):151–158.
34. Sakaguchi M, Inouye S. 2000. Systemic allergic reactions to gelatin included in vaccines as a stabilizer. Jpn J Infect Dis 53:189–195.
35. Naudie D, Bourne RB, Rorabeck CH, et al. 1999. Survivorship of the high tibial valgus osteotomy. A 10- to -22-year followup study. Clin Orthop Relat Res 367: 18–27.

Preparation and Characterization of Polyion Complex Micelles with a Novel Thermosensitive Poly(2-isopropyl-2-oxazoline) Shell via the Complexation of Oppositely Charged Block Ionomers†

Joon-Sik Park,‡ Yoshitsugu Akiyama,§ Yuichi Yamasaki,‡,|| and Kazunori Kataoka*,‡,||,⊥

Department of Materials Engineering, Graduate School of Engineering, The University of Tokyo, 7-3-1 Hongo, Bunkyo-ku, Tokyo 113-8656, Japan, Departments of Chemistry and Biology, University of Virginia, McCormick Road, Charlottesville, Virginia 22904, Center for NanoBio Integration, The University of Tokyo, 7-3-1 Hongo, Bunkyo-ku, Tokyo 113-8656, Japan, and Center for Disease Biology and Integrative Medicine, Graduate School of Medicine, The University of Tokyo, 7-3-1 Hongo, Bunkyo-ku, Tokyo 113-0033, Japan

Received May 22, 2006. In Final Form: September 5, 2006

Novel thermosensitive polyion complex (PIC) micelles were prepared in an aqueous medium based on the complexation of a pair of oppositely charged block ionomers, poly(2-isopropyl-2-oxazoline)-*b*-poly(amino acid)s (P*i*PrOx-*b*-PAA), containing thermosensitive P*i*PrOx segments. The controlled synthesis of P*i*PrOx-*b*-PAA was achieved via the ring-opening anionic polymerization of *N*-carboxyanhydrides (NCA) of either ϵ-benzyloxycarbonyl-L-lysine (Lys(Z)-NCA) or β-benzyl-L-aspartate (BLA-NCA) with ω-amino-functionalized P*i*PrOx macroinitiators and the subsequent deprotection reaction under acidic or basic conditions. Gel permeation chromatography (GPC) and ^{1}H NMR spectroscopy revealed that the syntheses of two block ionomers, poly(2-isopropyl-2-oxazoline)-*b*-poly(L-lysine) [P*i*PrOx-P(Lys)] and poly(2-isopropyl-2-oxazoline)-*b*-poly(aspartic acid) [P*i*PrOx-P(Asp)], proceeded almost quantitatively to give samples with a narrow molecular weight distribution ($M_w/M_n \leq 1.2$). The mixing of these two oppositely charged block ionomers in an aqueous medium led to the spontaneous formation of PIC micelles, which was confirmed by dynamic light scattering (DLS) and transmission electron microscopy (TEM). The PIC micelles were spherical particles with a narrow distribution in the range of the measured concentration (0.125−1 mg/mL) and were stable without any secondary aggregates. Furthermore, the PIC micelles had a constant cloud-point temperature (T_{cp}) of ~32 °C under physiological conditions regardless of the total concentration, suggesting that the concentration factor is almost negligible with respect to the T_{cp} of the micelles presumably because of the increased local concentration of the P*i*PrOx segments in the shell layer. These PIC micelles have a promising application as a size-regulated smart nanocontainer loading charged compounds as well as bearing a thermosensitive outer shell that is useful for physical affinity control.

Introduction

Recently, the self-assemblies of block copolymers have attracted an enormous amount of interest as potential materials in separation technology[1] and surface modification[2] and have promising carriers in drug delivery systems.[3,4] In particular, the use of polymeric micelles as drug carriers has numerous advantages[3] resulting from structural characteristics such as mesoscopic-scale size, core−shell structure, and thermodynamic stability. In particular, the polyion complex (PIC) micelles have opened the way to incorporate charged macromolecules of synthetic and biological origins, including proteins and nucleic acids, into the micelles.[5] The cores of PIC micelles could serve as nanoreservoirs for these charged compounds, allowing control of innate properties such as stability, solubility, and reactivity. A fundamental study of PIC micelle formation from a mixture of a series of oppositely charged block ionomers with poly(ethylene glycol) (PEG) as a hydrophilic segment, poly(ethylene glycol)-*b*-poly(L-lysine) [PEG-P(Lys)], and poly(ethylene glycol)-*b*-poly(aspartic acid) [PEG-P(Asp)] even revealed a unique molecular recognition process based on the length of the charged segments.[6] The PIC micelles entrapping enzymes in the core were also expected to be useful as functional materials such as nanometric-scale enzymatic reactors, which might be useful in the field of diagnostics and therapeutics.[7]

These interesting properties of PIC micelles as a functional supramolecular assembly may be enhanced when combined with a responsivity to external chemical and physical stimuli such as pH, magnetism, light, and heat. Of particular interest is the thermoresponsivity that can be a useful function in various applications including thermosensitive nanoreactors and drug delivery systems. Although there have been several studies on thermosensitive polymeric micelles with the potential to be a

† Part of the Stimuli-Responsive Materials: Polymers, Colloids, and Multicomponent Systems special issue.

* To whom correspondence should be addressed. E-mail: kataoka@bmw.t.u-tokyo.ac.jp. Tel: +81-3-5841-7138. Fax: +81-3-5841-7139.

‡ Department of Materials Engineering, Graduate School of Engineering, The University of Tokyo.

§ University of Virginia.

|| Center for NanoBio Integration, The University of Tokyo.

⊥ Center for Disease Biology and Integrative Medicine, Graduate School of Medicine, The University of Tokyo.

(1) (a) Nagarajan, R.; Barry, M.; Ruckenstein, E. *Langmuir* **1986**, *2*, 210. (b) Hurter, P. N.; Hatton, T. A. *Langmuir* **1992**, *8*, 1291.

(2) (a) Webber, S. E. *J. Phys. Chem.* **1998**, *102*, 2618. (b) Emoto, K.; Iijima, M.; Nagasaki, Y.; Kataoka, K. *J. Am. Chem. Soc.* **2000**, *122*, 2653. (c) Otsuka, H.; Nagasaki, Y.; Kataoka, K. *Curr. Opin. Colloid Interface Sci.* **2001**, *6*, 21.

(3) (a) Kataoka, K.; Kwon, G. S.; Yokoyama, M.; Okano, T.; Sakurai, Y. *J. Controlled Release* **1993**, *24*, 119. (b) Kataoka, K.; Harada, A.; Nagasaki, Y. *Adv. Drug Delivery Rev.* **2001**, *47*, 113. (c) Nishiyama, N.; Bae, Y. S.; Miyata, K.; Fukushima, S.; Kataoka, K. *Drug Discovery Today* **2005**, 2, 21.

(4) (a) Discher, D. E.; Eisenberg. A. *Science* **2002**, *297*, 967. (b) Discher, B. M.; Hammer, D. A.; Bates, F. S.; Discher, D. E. *Curr. Opin. Colloid Interface Sci.* **2000**, *5*, 125.

(5) (a) Harada, A.; Kataoka, K. *Macromolecules* **1995**, *28*, 5294. (b) Kabanov, A. V.; Bronich, T. K.; Kabanov, V. A.; Yu, K.; Eisenberg, A. *Macromolecules* **1996**, *29*, 6797. (c) Kakizawa, Y.; Kataoka, K. *Adv. Drug Delivery Rev.* **2002**, *54*, 203.

(6) (a) Harada, A.; Kataoka, K. *Science* **1999**, *283*, 65. (b) Harada, A.; Kataoka, K. *Macromolecules* **2003**, *36*, 4995.

(7) (a) Harada, A.; Kataoka, K. *Macromolecules* **1998**, *31*, 288. (b) Harada, A.; Kataoka, K. *J. Am. Chem. Soc.* **1999**, *121*, 9241. (c) Harada, A.; Kataoka, K. *J. Am. Chem. Soc.* **2003**, *125*, 15306. (d) Jaturanpinyo, M.; Harada, A.; Yuan, X.; Kataoka, K. *Bioconjugate Chem.* **2004**, *15*, 344.

10.1021/la061431j CCC: $37.00
Published on Web 11/10/2006

Scheme 1. Syntheses of Block Copolymers (P*i*PrOx-P(Lys(Z)) and P*i*PrOx-PBLA) and Deprotected Block Ionomers (P*i*PrOx-P(Lys) and P*i*PrOx-P(Asp))

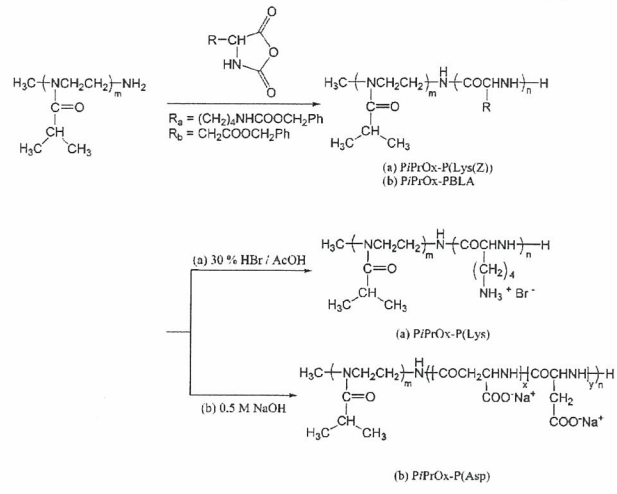

site-specific drug carrier based on poly(*N*-isopropylacrylamide) (PNIPAAm),[8] they have focused on the modulated amphiphilicity required to form the micelle with a hydrophobic inner core that is useful for the entrapment of hydrophobic therapeutic molecules such as anticancer drugs.[9] Little attention has been paid to the PIC micelles bearing a thermosensitive shell layer, though they have become even more attractive as an intelligent carrier of charged compounds utilizing temperature changes.

Of importance to the construction of PIC micelles with clear thermosensitivity are block ionomers composed of a hydrophilic segment with regulated thermosensitivity. In this regard, our recent findings of the quantitative cationic polymerization and selective end-functionalization of novel thermosensitive poly(2-isopropyl-2-oxazoline) (P*i*PrOx) telechelics are attractive.[10] The polymerization proceeded in a good controlled manner under optimum temperature conditions with appreciably narrow molecular weight distributions ($M_w/M_n \leq 1.03$). In particular, ω-amino-terminated P*i*PrOx (Me-P*i*PrOx-NH_2) allows the synthesis of biocompatible block ionomers based on poly(amino acids) because it can serve as an efficient macroinitiator to allow the ring-opening polymerization of *N*-carboxyanhydrides of protected amino acids (NCA), including ϵ-benzyloxycarbonyl-L-lysine (Lys(Z)-NCA) and β-benzyl-L-aspartate (BLA-NCA).

In this study, we established the novel synthetic route of two kinds of block ionomers composed of P*i*PrOx as a hydrophilic segment with either the oppositely charged poly(amino acid) segment as the other block (P*i*PrOx-P(Lys) or P*i*PrOx-P(Asp)) (Scheme 1). The stable and monodispersive PIC micelles were then prepared through the electrostatic interaction between cationic (P*i*PrOx-P(Lys)) and anionic (P*i*PrOx-P(Asp)) block ionomers in an aqueous medium (Scheme 2) to explore their thermosensitive behavior under physiological conditions using the turbidimetric method. These PIC micelles may offer promising applications as a size-regulated smart nanocontainer loading charged compounds as well as bearing the thermosensitive outer shell that is useful for physical affinity control.

(8) (a) Heskins, M.; Guillent, J. E.; James, E. J. *J. Macromol. Sci. Chem.* **1968**, *A2*, 1441. (b) Schild H. G. *Prog. Polym. Sci.* **1992**, *17*, 163.

(9) (a) Cammas, S.; Suzuki, K.; Sone, Y.; Sakurai, Y.; Kataoka, K.; Okano, T. *J. Controlled Release* **1997**, *48*, 157. (b) Chung, J. E.; Yokoyama, M.; Okano, T. *J. Controlled Release* **2000**, *65*, 93.

(10) (a) Park, J. S.; Akiyama, Y.; Winnik, F. M.; Kataoka, K. *Macromolecules* **2004**, *37*, 6786. (b) Diab, C.; Akiyama, Y.; Kataoka, K.; Winnik, F. M. *Macromolecules* **2004**, *37*, 2556.

Experimental Section

Materials. 2-Isopropyl-2-oxaxoline was synthesized from isobutyric acid (Wako Pure Chemical Industries, Ltd., Japan) and 2-aminoethanol (Wako Pure Chemical) as previously described.[10] Tetrahydrofuran (THF), *n*-hexane, *N*,*N*-dimethylformamide (DMF), and chloroform (Wako Pure Chemical) were purified by distillation following conventional procedures.[11] Trifluoroacetic acid, triethylamine, and acryloyl chloride were purchased from Wako Pure Chemicals and were used without further purification. ϵ-Benzyloxycarbonyl-L-lysine and β-benzyl-L-aspartate were purchased from the Peptide Institute, Inc., Japan, and used without further purification. Bis(trichloromethyl) carbonate (triphosgene) and 30% HBr/AcOH were purchased from Tokyo Kasei Kogyo Co., Ltd., Japan, and used without further purification. The synthesis of two NCAs (ϵ-benzyloxycarbonyl-L-lysine NCA (Lys(Z)-NCA) and β-benzyl-L-aspartate NCA (BLA-NCA)) was carried out by the Fuchs−Farthing method using triphosgene.[12] α-Methyl-ω-amino-poly(2-isopropyl-2-oxazoline) (Me-P*i*PrOx-NH_2, M_n = 4500, M_w/M_n = 1.03, functionality of ω-amino group = ca. 96%) was synthesized as previously described.[10a]

Techniques. The ^{1}H NMR spectra were recorded using a JEOL EX 300 spectrometer at 300 MHz. Chemical shifts were reported in ppm downfield from tetramethylsilane. The molecular weights and molecular weight distributions were determined using a GPC (TOSOH HLC-8220) system equipped with two TSK gel columns ($G4000H_{HR}$ and $G3000H_{HR}$) and an internal refractive index (RI) detector. The columns were eluted with DMF containing lithium bromide (10 mM) at a flow rate of 0.8 mL/min and were maintained at a temperature of 40 °C. The molecular weights were calibrated with poly(ethylene glycol) (PEG) standards (Polymer Laboratories, Ltd., U.K.). The UV−vis spectra were obtained using a V-550 UV/vis Jasco spectrophotometer. Transmission electron microscopy (TEM) was performed using a Hitachi H-7000 operating at an acceleration voltage of 75 kV. Dynamic light scattering (DLS) measurements were carried out using a DLS-7000 instrument (Otsuka Electronics Co., Ltd.). Vertically polarized light at a wavelength of λ_0 = 488 nm from an Ar ion laser was used as the incident beam. The average ζ-potential and light scattering intensity at 90° (SLS mode) were measured using a Zetasizer Nano particle analyzer, NanoZS (green badge, ZEN3500; Malvern, Ltd., Malvern, U.K.) with a green laser (λ = 532 nm).

Synthesis of α-Methyl-ω-acrylate-poly(2-isopropyl-2-oxazoline) (Me-P*i*PrOx-acrylate). For comparison with the thermoresponsive behavior of Me-P*i*PrOx-OH bearing a terminal hydrophilic ω-hydroxyl group, the ω-acrylate-terminated P*i*PrOx (Me-P*i*PrOx-acrylate) was synthesized by the conversion of the ω-hydroxyl group of Me-P*i*PrOx-OH. A 53 mg (0.011 mmol) sample of Me-P*i*PrOx-OH (M_n = 4500, M_w/M_n = 1.03) was dissolved in 0.75 mL of THF with triethylamine (0.0445 g, 0.44 mmol), and acryloyl chloride (0.0195 g, 0.22 mmol) in 0.25 mL of THF was added dropwise to the solution with stirring. The reaction temperature was maintained at 0 °C. After all of the acryloyl chloride was added, the reaction was allowed to continue with stirring for 2 h at 0 °C and for 24 h at room temperature in the dark. The triethylamine hydrochloride salts were then removed by filtration. The resulting solution was dialyzed against methanol and distilled water for 48 h with periodic bath changes to remove any unreacted compounds. The final dialysis product was lyophilized overnight using a freeze dryer to give Me-P*i*PrOx-acrylate (50 mg, ca. 94% yield). The characterization of Me-P*i*PrOx-acrylate was done by MALDI-TOF mass spectrometry (M_n = 4500, M_w/M_n = 1.03, Figure S1 in Supporting Information) and ^{1}H NMR spectroscopy (the conversion efficiency is ca. 80%, Figure S2 in Supporting Information).

Synthesis of Poly(2-isopropyl-2-oxazoline)-*b*-poly(ϵ-benzyloxycarbonyl-L-lysine) Copolymer (P*i*PrOx-P(Lys(Z)) (Run 1 in Table 1). ϵ-Benzyloxycarbonyl-L-lysine NCA (Lys(Z)-NCA; 81 mg, 0.26 mmol) dissolved in 1 mL of DMF was added to a solution of α-methyl-ω-amino-poly(2-isopropyl-2-oxazoline) (Me-P*i*PrOx-NH_2,

(11) Perrin, D. D.; Armarego, W. L. F.; Perrin, D. R. *Purification of Laboratory Chemicals*; Pergamon Press: Oxford, U.K., 1980.

Scheme 2. Schematic Model of the Formation of Thermosensitive Polyion Complex (PIC) Micelles from a Pair of Oppositely Charged Block Ionomers

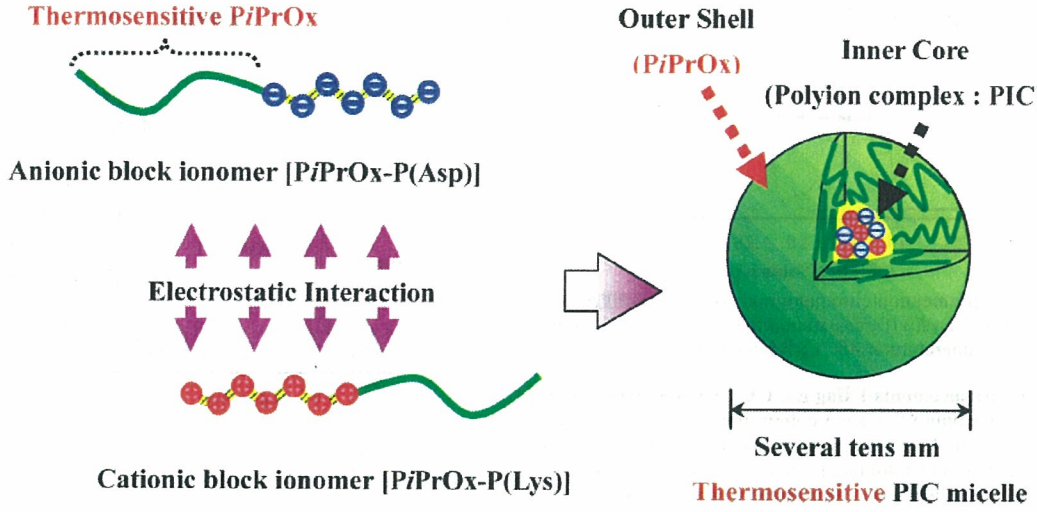

Table 1. Results of Block Copolymer Syntheses (P*i*PrOx-P(Lys(Z)) and P*i*PrOx-PBLA)

P*i*PrOx-P(Lys(Z))[a]								
macroinitiator [MI]			[Lys(Z)-NCA]$_0$				unit ratio[b]	
run	DP[b]	M_w/M_n[b]	[MI]$_0$	time (day)	yield (%)	M($\times 10^{-3}$)[b]	*m*:*n*	M_w/M_n[c]
1	40	1.03	60	4	82	17.6	40:50	1.2
2	40	1.03	80	4	78	21.5	40:79	1.2
P*i*PrOx-PBLA[d]								
macroinitiator [MI]			[BLA-NCA]$_0$				unit ratio[e]	
run	DP[e]	M_w/M_n[e]	[MI]$_0$	time (day)	yield (%)	M_n ($\times 10^{-3}$)[e]	*m*:*n*	M_w/M_n[e]
3	40	1.03	60	3	90	16.2	40:57	1.2
4	40	1.03	80	3	98	20.9	40:80	1.1

[a] Solvent, DMF; [Lys(Z)-NCA]$_0$, 0.1 mmol/mL (run 1), 0.133 mmol/mL (run 2); temp, 37.5 °C. [b] Estimated by ^{1}H NMR in DMSO at 50 °C. [c] Estimated by GPC in DMF containing 10 mM LiCl at 40 °C. [d] Solvent, CH_2Cl_2; [BLA-NCA]$_0$, 0.2 mmol/mL (run 3), 0.267 mmol/mL (run 4); temp, 37.5 °C. [e] Estimated by ^{1}H NMR in DMSO at 50 °C (run 3) and $CDCl_3$ at 25 °C (run 4).

$M_n = 4500$, $M_w/M_n = 1.03$) (20 mg, 0.0044 mmol) in 1 mL of DMF and stirred at 37.5 °C for 4 days under a dry argon atmosphere. The polymerization was monitored by IR spectrometry. After confirming the disappearance of the *N*-carboxyanhydride (NCA) monomers, the mixture was concentrated under reduced pressure and added to 300 mL of *n*-hexane. The precipitate was dissolved in 1 mL of chloroform, followed by reprecipitation into 200 mL of diethyl ether to give P*i*PrOx-P(Lys(Z)) (yield: 82% (83 mg)). The composition of P*i*PrOx-P(Lys(Z)) was determined by GPC and ^{1}H NMR in DMSO-d_6.

Synthesis of Poly(2-isopropyl-2-oxazoline)-*b*-poly(L-lysine) Copolymer (P*i*PrOx-P(Lys)). P*i*PrOx-P(Lys(Z)) (83 mg, 5.4 × 10^{-6} mmol) (run 1 in Table 1) was dissolved in 5 mL of trifluoroacetic acid and stirred for 0.5 h. The solution was then added to 10 mL of a 30 wt % solution of HBr in AcOH, and the reaction mixture was stirred for 2 h at room temperature. Finally, the reaction mixture was precipitated in *n*-hexane, and the product was isolated by repeated precipitations. The product was then redissolved in distilled water and dialyzed against distilled water using a Spectrapor dialysis membrane with a 3500 M_r molecular weight cutoff value. P*i*PrOx-P(Lys) was obtained as a white powder after lyophilization (yield: 78% (65 mg)).

Synthesis of Poly(2-isopropyl-2-oxazoline)-*b*-poly(aspartic acid) Copolymer (P*i*PrOx-P(Asp)). β-Benzyl-L-aspartate NCA (BLA-NCA; 66 mg, 0.26 mmol) dissolved in 1 mL of dichloromethane was added to a solution of α-methyl-ω-amino-poly(2-isopropyl-2-oxazoline) (Me-P*i*PrOx-NH_2, M_n = 4500, M_w/M_n = 1.03) (20 mg, 0.0044 mmol) in 1 mL of dichloromethane and stirred at 37.5 °C for 3 days under a dry argon atmosphere. A procedure similar to that for P*i*PrOx-P(Lys(Z)) was also adapted for P*i*PrOx-PBLA (run 3 in Table 1). P*i*PrOx-P(Asp) was then prepared from P*i*PrOx-PBLA by the removal of the benzyl groups in 0.5 N NaOH at room temperature (reaction time 5 h). (yield: 95% (55 mg)).

Preparation of Polyion Complex Micelles. P*i*PrOx-P(Lys) and P*i*PrOx-P(Asp) were separately dissolved in a Tris-HCl buffered solution (10 mM, pH 7.4) with or without a varying NaCl concentration of 10, 100, and 150 mM, respectively. After filtration through a 0.4 μm filter (MILLEX-VV, Millipore), the polyion complex micelles were prepared by mixing these solutions in an equal unit ratio of L-lysine and aspartic acid residues in the block copolymers (total concentration: 1.0 mg/mL).

Dynamic Light Scattering (DLS) Measurements. All samples were stored overnight before the measurements and used without further purification. All measurements were performed at 20 °C. Details of the data analysis procedure have been described eleswhere.[4a,13]

Transmission Electron Microscopy (TEM). For the observation of the size and distribution of the micellar particles, a drop of the sample solution (concentration = 0.125 mg/mL) was placed onto a 400 mesh copper grid coated with a 0.5 wt % poly(vinyl formal) aqueous solution. About 2 min after deposition, the grid was touched with filter paper to remove the surface water, followed by air drying. Negative staining was performed using a droplet of a 1 wt % uranyl acetate solution. The samples were air dried before the measurement.

(12) (a) Daly, H. W.; Poche, D. *Tetrahedron Lett.* **1988**, *29*, 5859. (b) Fasman, G. D.; Idelson, M.; Blout, E. R. *J. Am. Chem. Soc.* **1961**, *83*, 709.
(13) (a) Xu, R.; Winnik, M. A.; Hallett, F. R.; Riess, G.; Croucher, M. D. *Macromolecules* **1991**, *24*, 87. (b) Harada, A.; Kataoka, K. *Macromolecules* **1998**, *31*, 288.

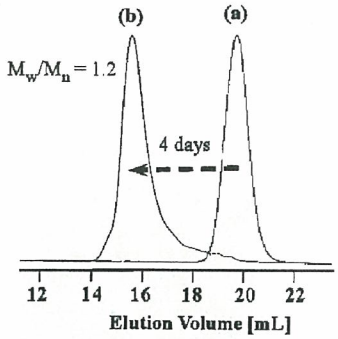

Figure 1. Gel permeation chromatograms of (a) Me-P*i*PrOx-NH_2 and (b) P*i*PrOx-P(Lys(Z)) (PEG standard; eluant, DMF (containing 10 mM LiCl); temperature, 40 °C; RI detection).

Turbidity Measurements Using the UV−Vis Spectrophotometer. The cloud points (T_{cp}) were determined by the spectrophotometric detection of the changes in the transmittance ($\lambda = 500$ nm) of the aqueous polymer solutions heated at a constant rate (0.5 °C min^{-1}). The samples were thermostated using a temperature-controlled circulating water bath. Cloud-point values of the polymer solutions were determined as the temperature corresponding to a 10% decrease in the optical transmittance.

Results and Discussion

Synthesis of Block Copolymers. In this study, ω-amino-terminated poly(2-isopropyl-2-oxazoline) (Me-P*i*PrOx-NH_2) (M_n = 4500, M_w/M_n = 1.03) was employed as a macroinitiator for the anionic ring-opening polymerization of NCA to form the block copolymers of P*i*PrOx and protected poly(amino acid) (P*i*PrOx-P(Lys(Z)) or P*i*PrOx-PBLA). The synthesized block copolymers were characterized by GPC and ^{1}H NMR as summarized in Table 1. Figure 1 shows the GPC profiles of the macroinitiator (Me-P*i*PrOx-NH_2) and the block copolymer (P*i*PrOx-P(Lys(Z))). After block copolymerization was carried out for 4 days, the peak shifted to a smaller elution volume because of an increase in the molecular weight. No peak of the macroinitiator remained, indicating the high efficiency of the block copolymerization. Figure 2 shows the ^{1}H NMR spectra of the block copolymer before (Figure 2a) and after (Figure 2b) the deprotection of the ε-benzyloxycarbonyl groups under the acidic conditions (30% HBr/AcOH) for run 1 in Table 1. Comparing the peak integral ratio of the methyl protons of P*i*PrOx ($(CH_3)_2$: δ 1.0) and the methylene protons of the ε-benzyloxycarbonyl group of P(Lys(Z)) ($CH_2C_6H_5$: δ 4.9), the DP of Lys(Z) was calculated to be 50. For P*i*PrOx-P(Lys) in Figure 2b, the peak integral ratio of the methyl protons of P*i*PrOx ($(CH_3)_2$: δ 1.0) and α-methine protons of P(Lys) (CO*CH*NH: δ 4.2) was measured in order to calculate the DP that was determined to be 52. It was confirmed from the similar DP values of lysine units for P*i*PrOx-P(Lys(Z)) and P*i*PrOx-P(Lys) that neither the loss of the lysine repeating units by backbone scission nor cleavage of the amide group to a secondary amino group in the side chain of the P*i*PrOx block occurred during the deprotection reaction. On the basis of these results, it was ascertained that the polymerization of Lys(Z)-NCA was successfully accomplished using the ω-amino-terminated P*i*PrOx macroinitiator: the polydispersity indices were about 1.2, and the experimental value of the degree of polymerization (DP) was close to the value predicted from the initial monomer/macroinitiator ratio (60/1). The P*i*PrOx-P(Lys) block ionomers (P*i*PrOx; M_n = 4500 g/mol) with different DP values of the P(Lys) segments, 52 and 82, are abbreviated 45C52 and 45C82, respectively.

In a similar fashion, the synthesis of P*i*PrOx-PBLA was performed as shown in Table 1 (runs 3 and 4). From the GPC

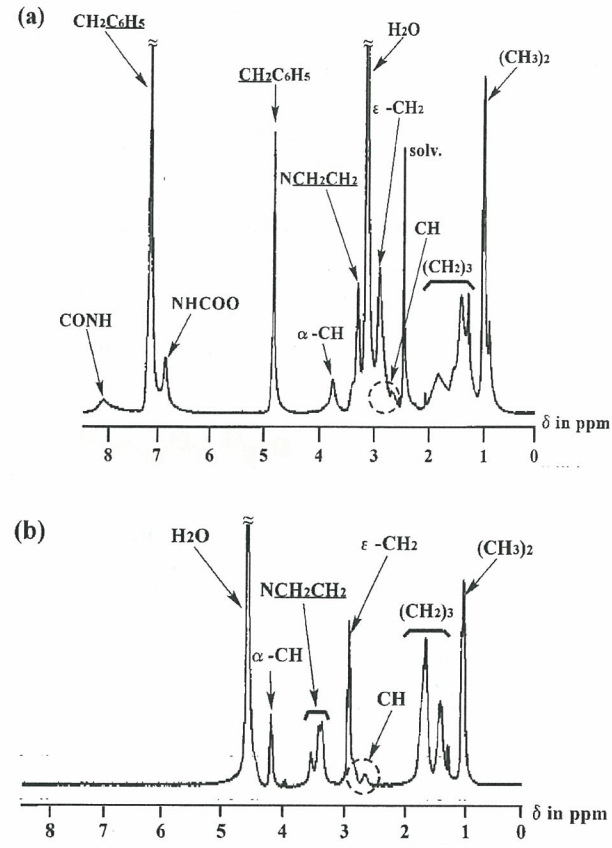

Figure 2. ^{1}H NMR spectra of (a) P*i*PrOx-P(Lys(Z)) in DMSO-d_6 at 50 °C and (b) P*i*PrOx-P(Lys) in D_2O at 20 °C.

of the obtained P*i*PrOx-PBLA (run 3 in Table 1, Figure S3 in Supporting Information), a unimodal peak was also observed in the reaction mixture after 3 days as in the case of P*i*PrOx-P(Lys-(Z)). To assign the composition of P*i*PrOx-PBLA, the ^{1}H NMR was measured in DMSO-d_6 (run 3) (Figure S4 in Supporting Information). From the peak integral ratio of the methyl protons of P*i*PrOx ($(CH_3)_2$: δ 1.0) to the benzyl protons of PBLA ($COOCH_2C_6H_5$: δ 7.2), the DP of BLA was determined to be 57. The ^{1}H NMR spectrum of P*i*PrOx-P(Asp) in D_2O, obtained after deprotection of the benzyl groups of P*i*PrOx-PBLA (run 3), is also shown in Figure S5 of Supporting Information. Although some of the peaks assigned to the methylene protons of the α,β linkages of P(Asp) (δ 2.7)[14] were superposed on a broad peak assigned to the methine proton of the isopropyl group of P*i*PrOx (δ 2.4−2.9), the DP (53) calculated from the integral ratio of the methyl protons of P*i*PrOx ($(CH_3)_2$: δ 1.0) to the methylene protons of the α,β linkages of P(Asp) (δ 2.7) was also in a good agreement with the result (DP = 57) for P*i*PrOx-PBLA. The P*i*PrOx-P(Asp) block ionomers (P*i*PrOx; M_n = 4500 g/mol) with different DP values of the P(Asp) segments, 53 and 76, are abbreviated 45A53 and 45A76, respectively.

Preparation of Polyion Complex Micelles. The PIC micelles were formed by mixing 1.0 mg/mL Tris-HCl solutions of P*i*PrOx-P(Lys) and P*i*PrOx-P(Asp) under stoichiometric conditions in which the unit ratio of the L-lysine in P*i*PrOx-P(Lys) and aspartate in P*i*PrOx-P(Asp) was unity. This procedure of PIC micelle formation by the simple mixing of a pair of oppositely charged

(14) (a) Yokoyama, M.; Miyauchi, M.; Yamada, N.; Okano, T.; Sakurai, Y.; Kataoka, K.; Inoue, S. *J. Controlled Release* **1990,** *11,* 269. (b) Yokoyama, M.; Inoue, S.; Kataoka, K.; Yui, N.; Okano, T.; Sakurai, Y. *Makromol. Chem.* **1989,** *190,* 2041.

Table 2. Size and Polydispersity Index Values of the PIC Micelles

samples	concentration (mg/mL)	D_T[a] (10^{-7}cm^2/s)	μ_2/Γ^2 [a]	R_h[b] (nm)	diameter (nm) mean cumulative[a]	diameter (nm) z-weighted[c]	d_w/d_n[c]
45C52/45A53	1	1.306	0.078		36.2	37.0 ⊥ 8.4	1.16
	0.5	1.237	0.062	18.0	36.6	38.8 ± 7.7	1.15
	0.25	1.218	0.121		37.2	41.2 ± 13.1	1.21
	0.125	1.208	0.178		37.7	41.3 ⊥ 16.2	1.19
45C82/45A76	1	0.819	0.044		39.6	41.0 ± 8.7	1.11
	0.5	0.833	0.075	22.6	39.5	42.6 ± 12.0	1.17
	0.25	0.823	0.059		40.0	42.6 ⊥ 12.9	1.17
	0.125	0.822	0.044		40.1	41.8 ± 9.9	1.13

45C52/45A53 (1 mg/mL)	D_T[a] (10^{-7}cm^2/s)	μ_2/Γ^2 [a]	diameter (nm) mean cumulative[a]	diameter (nm) z-weighted[c]	d_w/d_n[c]
10 mM NaCl	1.134	0.069	32.6	34.9 ± 9.1	1.15
100 mM NaCl	1.107	0.065	33.2	35.8 + 9.3	1.16
150 mM NaCl	1.048	0.094	36.6	37.6 ⊥ 8.8	1.13

[a] Obtained by cumulant analysis of dynamic light scattering (DLS). [b] Determined from the diffusion coefficient at infinite dilution (D_0) using the Stokes–Einstein equation. [c] Calculated by the histogram method. (d_w and d_n denote the weight- and number-average diameters, respectively.)

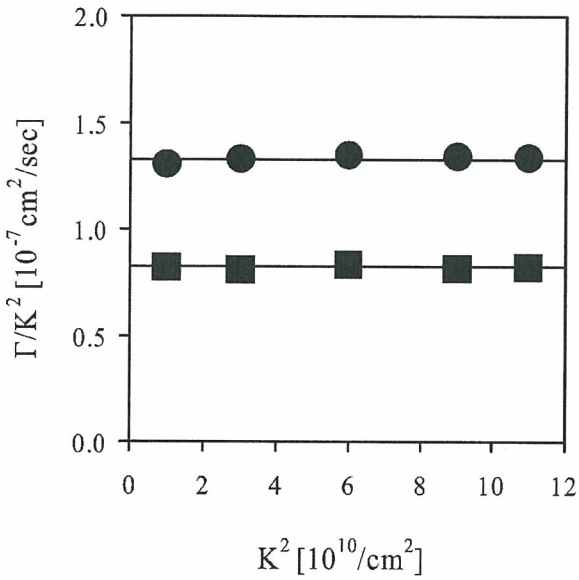

Figure 3. Relationship between the scaled average characteristic line width (Γ/K^2) and the magnitude of the scattering vector (K^2) for PIC micelles (45C52/45A53, ●; 45C82/45A76, ■; total concentration, 1.0 mg/mL; temperature, 20 °C; detection angles, 30, 60, 90, 120, and 150°; solvent, 10 mM Tris-HCl).

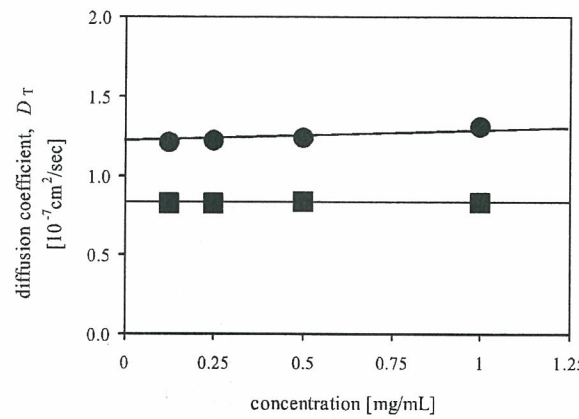

Figure 4. Plots of the translational diffusion coefficient (D_T) vs the total concentration of PIC micelles (45C52/45A53, ●; 45C82/45A76, ■; (temperature, 20 °C; detection angle, 90°; solvent, 10 mM Tris-HCl).

block ionomers had previously been established by our group for the PEG-P(Lys) and PEG-P(Asp) pair.[5a] The prepared solution was stored overnight in the refrigerator before DLS characterization.

Two pairs of PIC micelles were prepared by mixing the P*i*PrOx-based block ionomers with different charge lengths (Table 2): one comprising 45C52 where the unit number of L-lysine is 52 and 45A53 with the unit number of aspartate of 53 and the other comprising 45C82 where the unit number of L-lysine is 82 and 45A76 with the unit number of aspartate of 76. To investigate the shape as well as the size of the PIC micelles, angle-trace DLS measurements were carried out at 30, 60, 90, 120, and 150° detection angles at 20 °C. The sufficiently low temperature condition (20 °C) had to be adapted for all of the sample measurements, excluding the unexpected change in the shape or size of the PIC micelles, possibly derived from the collapse of the P*i*PrOx segments around the phase-transition temperature. Figure 3 shows the relationship between the scaled average of the scattering characteristic line width (Γ/K^2) and the magnitude of the scattering vector (K^2) at a concentration of 1 mg/mL. The Γ/K^2 values of the PIC micelles formed between P*i*PrOx-P(Lys) and P*i*PrOx-P(Asp) were independent of the detection angle in all cases. These results agreed with the fact that the Γ/K^2 values should be independent of the detection angle in the case of spherical particles. Because the angular dependence of Γ/K^2 was almost negligible, the following DLS measurements were performed at a 90° detection angle.

Figure 4 shows the concentration dependence of the diffusion coefficient (D_T). The PIC micelles were prepared by mixing the solutions of P*i*PrOx-P(Lys) and P*i*PrOx-P(Asp) (45C52/45A53 and 45C82/45A76 in Table 2) with diluting concentrations from 1 to 0.125 mg/mL under an electrostatically neutralized condition (1:1 unit ratio of L-lysine and aspartate residues). It is obvious that the diffusion coefficients were almost independent of the concentrations of both 45C52/45A53 and 45C82/45A76, indicating that the change in the total concentration induces no formation of secondary aggregates. It is likely that the P*i*PrOx shell layer may prevent the clustering of the micelles due to a steric repulsion mechanism, which is consistent with the formation of a core–shell structure. The diffusion coefficient at infinite dilution D_0 was then determined to be 1.187×10^{-7} cm^2/s (from 45C52/45A53 in Table 2) and 0.822×10^{-7} cm^2/s (from 45C82/45A76 in Table 2), respectively, for the 45C52/45A53 and 45C82/45A76

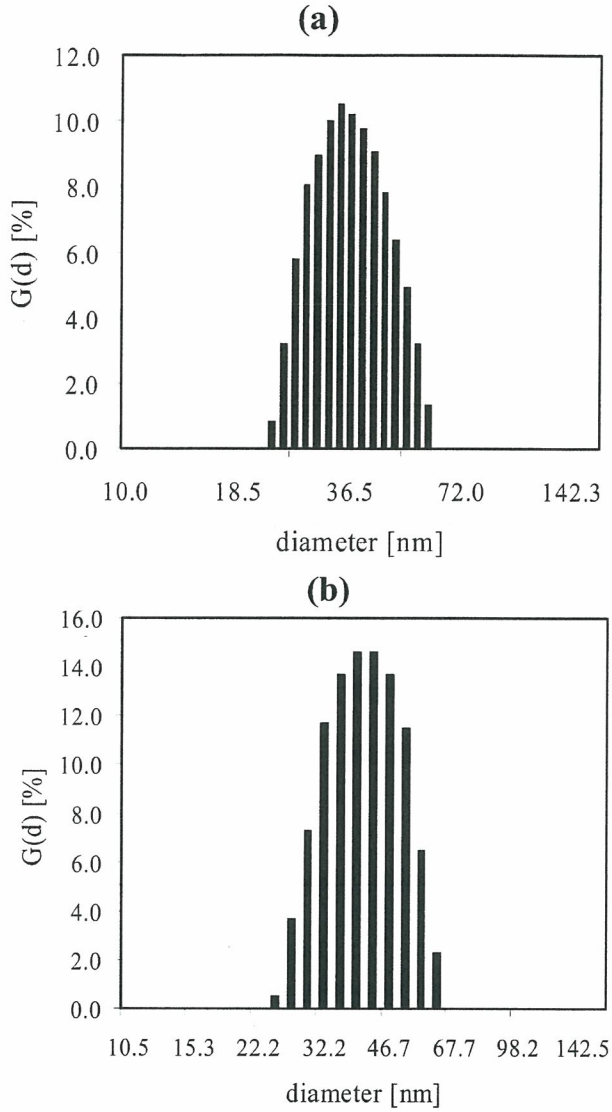

Figure 5. Γ-averaged size distribution analyzed by the histogram method for PIC micelles: (a) 45C52/45A53 and (b) 45C82/45A76 (total concentration, 1.0 mg/mL; temperature, 20 °C; detection angle, 90°; solvent, 10 mM Tris-HCl).

systems. From the obtained D_0 value, values of the hydrodynamic radius (R_h) were calculated to be 18.0 and 22.6 nm using the Stokes−Einstein equation. Obviously, the R_h values slightly increased with an increase in the length of the charged segments. The polydispersity indices (μ_2/Γ^2) (Table 2) were small enough to consider that the micelles have a narrow size distribution. This narrow size distribution is in good agreement with the result of the independence of the Γ/K^2 value versus the detection angle, as shown in Figure 3.

Figure 5 shows the Γ-averaged size distribution of the polyion complex micelles (1 mg/mL) obtained from the histogram analysis of the DLS data at 20 °C. It was confirmed from the size distribution profiles that the micelles prepared were unimodal with average diameters of 37.0 ± 8.4 and 41.0 ± 8.7 nm, respectively (Figure 5a and b for the 45C52/45A53 and 45C82/45A76 systems). These were in good agreement with the mean cumulative diameters (36.2 and 39.6 nm) and R_h values (18.0 and 22.6 nm) calculated from the cumulant analysis. All of the data including the polydispersity index (d_w/d_n) values obtained from this histogram method are also summarized in Table 2.

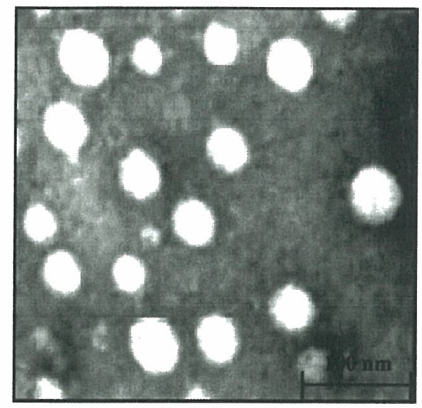

Figure 6. TEM image of PIC micelles formed from 45C52 and 45A53 in distilled water at room temperature (concentration, 0.125 mg/mL; negative staining by a 1 wt % uranyl acetate solution).

Furthermore, it was confirmed that monodisperse spherical particles with an ~40 nm diameter were clearly observed in the TEM image of the PIC micelles from 45C52/45A53 prepared in distilled water (Figure 6).

The electrophoretic mobility of the PIC micelle (45C52/45A53) was also determined to be −0.04745 ± 0.0105 μm cm/Vs on the basis of laser-Doppler electrophoresis. The average ζ-potential was then calculated from this value using the Smoluchowski equation.[5a] The calculated average ζ-potential of the PIC micelles had an extremely small absolute value (−0.6690 ± 0.148 mV), indicating the shielding of the PIC core by the electrically neutral shell of the P*i*PrOx segments.

On the basis of the results of the DLS, TEM, and ζ-potential described above, it is reasonable to conclude that the micelles having the PIC core were surrounded by P*i*PrOx as the shell layer and were stably dispersed with a narrow, unimodal distribution in an aqueous entity at 20 °C. It is known that the stability of the polyion complex is strongly affected by the ionic strength of the medium (i.e., destabilized with an increase in the ionic strength due to electrostatic shielding[15]). The effect of the ionic strength on the stability of the PIC micelles was estimated by measuring the size of the PIC micelle solutions (1 mg/mL) under several NaCl concentrations. The diffusion coefficients (D_T) remained constant almost up to the 150 mM NaCl concentration value, viz., near physiological conditions, meaning that the stability of the PIC micelles is sufficient under the measured ionic strengths (Table 2 and Figure 7a−c).

Determination of the Cloud Points (T_{cp}). As the first step in our study of the thermoresponsive behavior of the P*i*PrOx-based PIC micelles, we examined in detail the cloud-point (T_{cp}) values of the P*i*PrOx oligomer solutions. It was necessary to select two parameters, such as the oligomer and NaCl concentrations, when considering the future application of the PIC micelles under physiological conditions. In addition, ω-acrylate-terminated P*i*PrOx (Me-P*i*PrOx-acrylate) was prepared by end capping the ω-hydroxyl group of Me-P*i*PrOx-OH in order to explore the effects of the terminal end groups on T_{cp}, which are presumably pronounced for the oligomer solutions.

The open (in the absence of NaCl) and closed (in the presence of 150 mM NaCl) symbols in Figures 8a and b show the turbidity changes in the aqueous solutions of Me-P*i*PrOx-OH (M_n = 4500, M_w/M_n = 1.03) (square symbols) and Me-P*i*PrOx-acrylate (M_n = 4500, M_w/M_n = 1.03) (circle symbols) bearing the same chain length as that used in the synthesis of the block ionomers under

(15) (a) Abe, K.; Ohno, H.; Tsuchida, E. *Makromol. Chem.* **1977**, *178*, 2285. (b) Tsuchida, E.; Osada, Y.; Ohno, H. *J. Macromol. Sci. Phys.* **1980**, *B17*, 683.

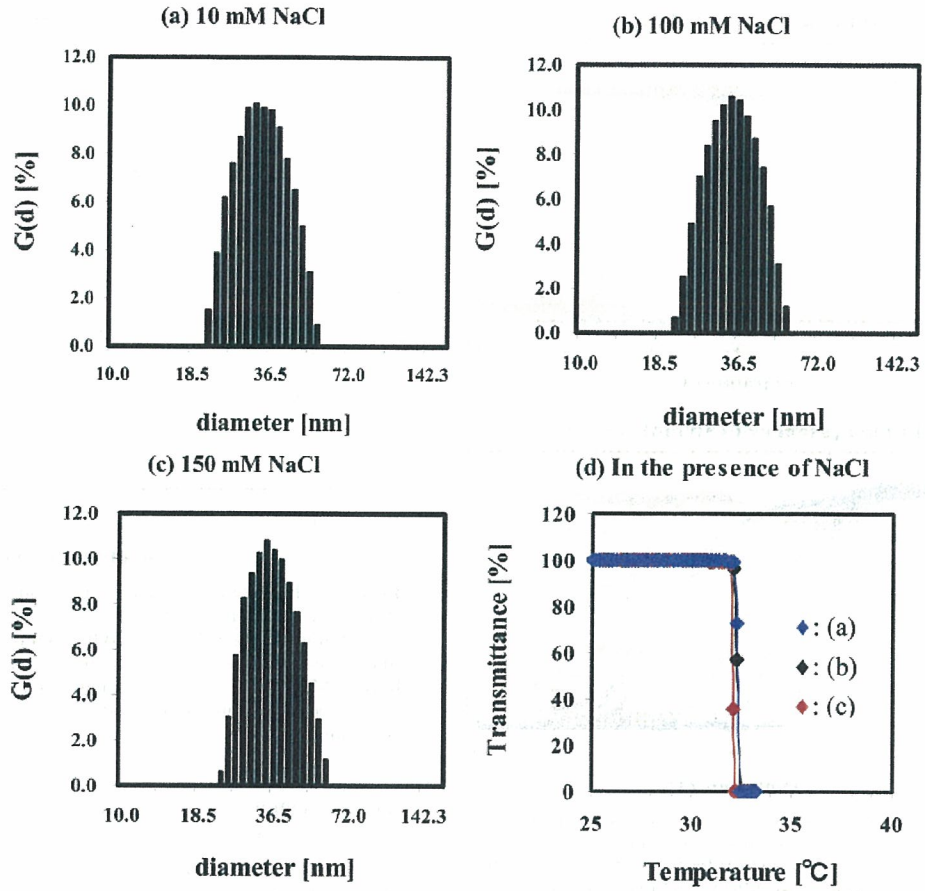

Figure 7. Γ-averaged size distribution analyzed by the histogram method for 45C52/45A53 with different NaCl concentrations: (a) 10, (b) 100, and (c) 150 mM. (d) Respective transmittance changes at 500 nm as a function of temperature (total concentration, 1.0 mg/mL; temperature, 20 °C; detection angle, 90°; solvent, 10 mM Tris-HCl; rate, 0.5 °C/min).

several concentrations (1−10 mg/mL). The T_{cp} values of Me-P*i*PrOx-acrylate, dissolved in 10 mM Tris-HCl buffer (pH 7.4), exhibited a remarkable dependence on the concentrations of both the oligomer and NaCl. The transmittance curves become duller by shifting to a higher temperature region as a result of the decreasing concentration of the oligomer solutions. Obviously, more than a 5 °C decrease in T_{cp} was observed at every oligomer concentration by adding 150 mM NaCl to the solution (Figures 8 and 9) Also, there was a gradual decrease in the T_{cp} at each oligomer concentration with an increase in the NaCl concentration (10, 100, 150 mM) (Figure 9) Alternatively, all of the ω-hydroxyl-terminated P*i*PrOx oligomers (Me-P*i*PrOx-OH) exhibited a sharp thermoresponsivity in the relatively higher temperature region (44−51 °C) compared to that of the Me-P*i*PrOx-acrylate, and the dependency of T_{cp} on the oligomer and NaCl concentrations was less pronounced. As the NaCl concentration increased from 0 to 150 mM, the decrease in the T_{cp} of Me-P*i*PrOx-OH was only in the range of a few degrees (Figures 8 and 9).

Note that turbidimetric behavior similar to that of P*i*PrOx has also been observed for poly(*N*-isopropylacrylamide) (PNIPAAm), a typical thermosensitive polymer as well as the chemical isomer of P*i*PrOx, at least in a similar molecular weight ($M_n \leq$ ca. 10 000) range. In particular, the LCST values of the end-functionalized PNIPAAm oligomers ($M_n \leq$ ca. 10 000) were found to have a significant dependence on either the hydrophilic or hydrophobic property of the terminal end group. For instance, ω-hydroxyl-terminated PNIPAAm with lower molecular weight from 3300 to 8000 demonstrated even higher LCST values of ca. 36−50 °C.[16b,c] This was considered to be a result of the comparatively enhanced hydrating contribution of hydrophilic ω-hydroxyl groups in the PNIPAAm oligomers, compared to that for those of higher molecular weight in which the ratio of the ω-terminal hydroxyl groups to the backbone is lower. In contrast, PNIPAAm with hydrophobic terminal ends, such as alkyl, phenyl, and pyrenyl groups, had LCST values shifted toward lower temperatures, which were quite pronounced with decreasing molecular weight.[16a,b,d−g] Moreover, the PNIPAAm oligomers with hydrophilic terminal ends showed relatively sharp transitions, whereas those of the hydrophobic terminal ends had a tendency toward early onset as well as also decreasing in their cloud-point curves, presumably resulting from the difference in the rate of aggregation.[16g] On the basis of these results from the PNIPAAm oligomer solutions, a similar explanation could be adapted for the higher T_{cp} values exhibiting a sharper transition of Me-P*i*PrOx-OH with the hydrophilic ω-hydroxyl groups than those of Me-P*i*PrOx-acrylate with hydrophobic ω-acrylate groups. As far as the notable dependency of T_{cp} of the P*i*PrOx oligomers on the NaCl concentration, this could be understood through the well-known "salting-out" effect of NaCl,[17] as also observed in previous studies of polyoxazolines including P*i*PrOx.[18] The T_{cp} values of

(16) (a) Chung, J. E.; Yokoyama, M.; Suzuki, K.; Aoyagi, T.; Sakurai, Y.; Okano, T. *Colloids Surf., B* **1997**, *9*, 37. (b) Chung, J. E.; Yokoyama, M.; Aoyagi, T.; Sakurai, Y.; Okano, T. *J. Controlled Release* **1998**, *53*, 119. (c) Kohori, F.; Sakai, K.; Aoyagi, T.; Yokoyama, M.; Sakurai, Y.; Okano, T. *J. Controlled Release* **1998**, *55*, 87. (d) Xia, Y.; Yin, X.; Burke, N. A. D.; Stöver, H. D. H. *Macromolecules* **2005**, *38*, 5937. (e) Duan, Q.; Miura, Y.; Narumi, A.; Shen, X.; Sato, S.-I.; Satoh, T.; Kakuchi, T. *J. Polym. Sci., Part A: Polym. Chem.* **2006**, *44*, 1117. (f) Furyk, S.; Zhang, Y.; Ortiz-Acosta, D.; Cremer, P. S.; Bergbreiter, D. E. *J. Polym. Sci., Part A: Polym. Chem.* **2006**, *44*, 1492. (g) Xia, Y.; Burke, N. A. D.; Stöver, H. D. H. *Macromolecules* **2006**, *39*, 2275.

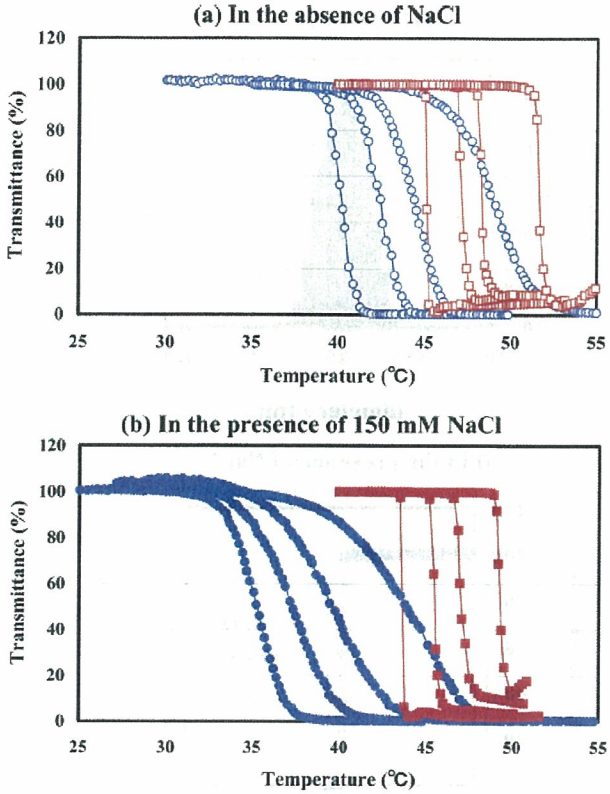

Figure 8. Transmittance changes at 500 nm as a function of temperature under different oligomer concentrations (1−10 mg/mL): (a) in the absence of NaCl (Me-P*i*PrOx-acrylate, $M_n = 4500$, $M_w/M_n = 1.03$; open circle), Me-P*i*PrOx-OH ($M_n = 4500$, $M_w/M_n = 1.03$; open square) and (b) in the presence of 150 mM NaCl (Me-P*i*PrOx-acrylate, solid circle; Me-P*i*PrOx-OH, solid square); 10 mM Tris-HCl buffered solution (pH 7.4); rate, 0.5 °C/min).

the respective P*i*PrOx oligomer solutions decrease with increasing concentration of NaCl up to 150 mM. In particular, the NaCl concentration effect on the decreasing T_{cp} values of Me-P*i*PrOx-OH was relatively alleviated compared to that of the Me-P*i*PrOx-acrylate, as a result of the existence of a hydrophilic hydroxyl group at the ω-terminal end (Figures 8 and 9). In other words, it was obvious that the salting-out effect of NaCl to decrease the affinity or solubility power of water against the hydrophilic carbonyl groups at the side chain of the Me-P*i*PrOx-OH oligomer solutions was reduced by the strong hydrating contribution of the terminal ω-hydroxyl groups.

Interestingly, the T_{cp} value of neither the 45C52 nor the 45A53 block ionomer solution both in the absence and the presence of 150 mM NaCl was detected in the measured temperature range up to 75 °C, suggesting the strong hydrating effect of the ionized groups at the side chains of a charged block segment of ionomers (Figure 10a and b). Although there is also possibility for the block ionomer systems to form nanometer-scale micelles composed of a hydrophilic charged outer shell and a hydrophobic P*i*PrOx inner core resulting from aggregation among the P*i*PrOx oligomers collapsed over the phase-separation temperature, it was ascertained from the static light scattering (SLS) measurement that no evidence of micellar formation, such as an increase in the light scattering intensity, was observed for the respective

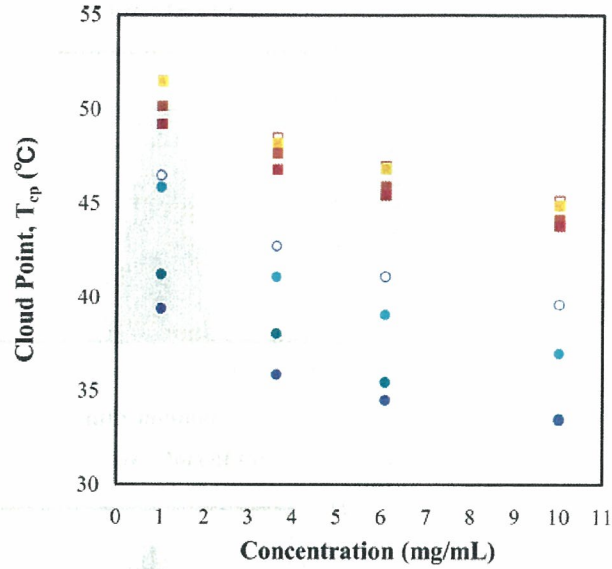

Figure 9. Plots of the changes in the cloud point (T_{cp}) determined from Figure 8 as a function of the respective oligomer concentration (1−10 mg/mL) (Me-P*i*PrOx-acrylate with 0, open circle; 10, solid light-green dot; 100, dark-green solid dot; and 150 mM NaCl, solid blue dot; Me-P*i*PrOx-OH with 0, open square; 10, light-orange solid square; 100, medium-orange solid square; and 150 mM NaCl, red solid square).

ionomer solutions in the measured temperature range (25−75 °C) (data not shown).

We next investigated the thermoresponsive behavior of P*i*PrOx under the formation of PIC micelles. Figure 10a also shows the transmittance changes in the 45C52/45A53 PIC micelles under several total concentrations (0.125, 0.25, 0.5, and 1 mg/mL; 10 mM Tris-HCl buffered solution (pH 7.4) in the absence of NaCl). The results showed a unique characteristic of the PIC micelles. Indeed, the T_{cp} values for the PIC micelles were observed to shift remarkably to a lower temperature than for the P*i*PrOx oligomers (Me-P*i*PrOx-OH and Me-P*i*PrOx-acrylate). Furthermore, all of the micelles with different total concentrations underwent an agglomeration even at a same constant temperature of ca. 33 °C. It was already confirmed in Table 2 and Figure 4 that the diffusion coefficients (D_T) and hence the cumulative average diameters of the PIC micelles remained almost constant under the wide concentration conditions down to 0.125 mg/mL at 20 °C, indicating that the micelles stably exist in the measured concentration region (0.125−1 mg/mL). In addition, the transmittance changes at a constant total concentration (1 mg/mL) but containing different NaCl concentrations up to 150 mM, as was also observed as shown in Figure 7d. The T_{cp} values of the PIC micelles coexisting with NaCl also exhibited a similar temperature, ca. 32 °C, which is similar to that in the absence of NaCl regardless of the NaCl concentration up to 150 mM. Moreover, the turbidimetric behavior of the 45C52/45A53 micelles in the presence of 150 mM NaCl was also investigated by diluting the total concentration from 1 to 0.125 mg/mL (Figure 10b). All of the micelles also showed a turbidity near the constant temperature of ca. 32 °C, and the changing behavior of the transmittance curves was similar to that in Figure 10a. Concerning the 45C52/45A53 micelles under 0.125 mg/mL, it was notable that the turbidimetric curve was rather broadly decreasing with increasing temperature compared to the initial sharp responsivity, obviously resulting from the dependence on the rate of temperature increase (Figure S6 in Supporting Information).

(17) (a) Eeckman, F.; Amighi, K.; Moës, A. J. *Int. J. Pharm.* **2001**, *222*, 259. (b) Freitag, R.; Garret-Flaudy, F. *Langmuir* **2002**, *18*, 3434. (c) Liu, X. M.; Wang, L. S.; Wang, L.; Huang, J.; He, C. *Biomaterials* **2004**, *25*, 5659.

(18) (a) Lin, P.; Pearce, E. M.; Kwei, T. K. *J. Polym. Sci., Part B: Polym. Phys.* **1988**, *26*, 603. (b) Uyama, H.; Kobayashi, S. *Chem. Lett.* **1992**, 1643.

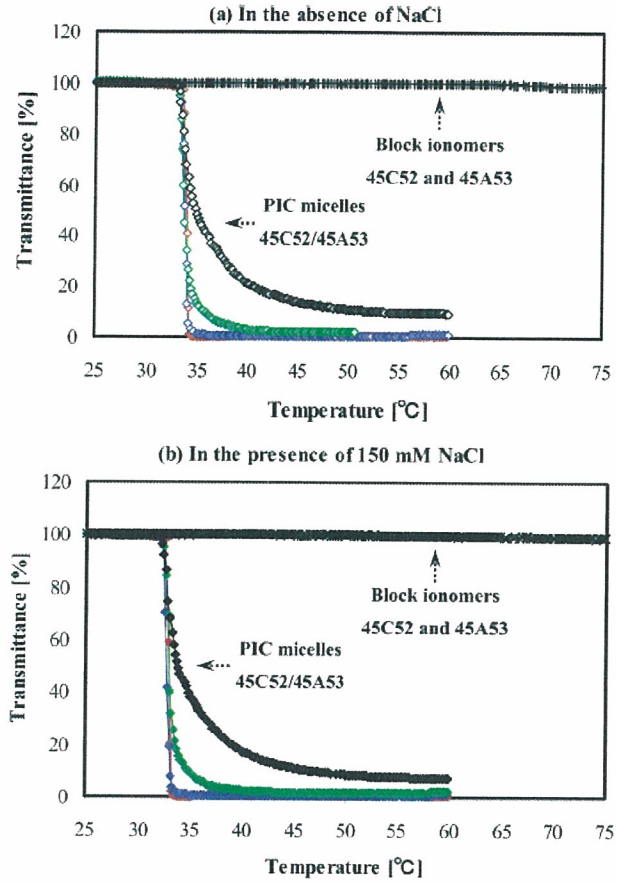

Figure 10. Transmittance changes at 500 nm as a function of temperature for oppositely charged block ionomers (45C52 and 45A53) and their PIC micelles (45C52/45A53): (a) in the absence of NaCl: block ionomers, +; PIC micelles (◇, 0.125 mg/mL; open green diamond, 0.25 mg/mL; open blue diamond, 0.5 mg/mL; and open red diamond, 1 mg/mL) and (b) in the presence of 150 mM NaCl: block ionomers, ×; PIC micelles (◆, 0.125 mg/mL; solid green diamond, 0.25 mg/mL; solid blue diamond, 0.5 mg/mL; and open red diamond, 1 mg/mL); 10 mM Tris-HCl buffered solution (pH 7.4); rate, 0.5 °C/min.

It should be noted that the T_{cp} values for the PIC micelles significantly shifted to a lower temperature (ca. 32−33 °C) when comparing two end-functionalized P*i*PrOx oligomers (Me-P*i*PrOx-OH and Me-P*i*PrOx-acrylate) and, in addition, were almost constant regardless of the total concentration of the system with or without NaCl (≤150 mM). It is reasonable to suggest that the remarkable decrease in T_{cp} may be related to the high local concentration of the P*i*PrOx segments on micelles with an appreciable increase in the apparent molecular weight. To put it more concretely, whereas the P*i*PrOx oligomer solutions were significantly related to the intermolecular aggregation behavior through the notable concentration-dependent dehydration process with increasing temperature, the supramolecular assembly, such as PIC micelles with densely packed outer shells, may prefer rapid intramicellar aggregation with an accelerated dehydration process resulting from the high local concentration of the micelles' shell layer. As a result, the T_{cp} values for the PIC micelles could be appreciably shifted to a lower temperature (ca. 32 °C) even rarely depending on the total concentration including NaCl up to 150 mM. In addition, another possible factor is also considered to be the effect of terminal end groups. The ω terminal groups of the P*i*PrOx oligomers, fixed on the shell surface of the present PIC micelles, could not be expected to interfere with the shifts in T_{cp}. However, it seemed that the hydrophobic methyl groups at the α-terminal ends of the P*i*PrOx oligomers, accumulated on the outermost micelle surfaces through self-assemblies among block ionomers, were also connected with the decreasing T_{cp} of the PIC micelles. As appreciated from the fact that the T_{cp} of Me-P*i*PrOx-acrylate with hydrophobic groups at both terminal ends decreased at a high rate with increasing concentration when comparing Me-P*i*PrOx-OH with the hydrophilic ω-hydroxyl ends, the T_{cp} of PIC micelles could be affected by the hydrophobic methyl groups existing on the outermost micelles surfaces. A similar result is that the presence of the hydrophilic or hydrophobic groups on the outermost surface of the polymeric micelles strongly influenced the shift in the LCST values of the micelles, which was also observed in the micelle system composed of the thermosensitive PNIPAAm outer shell and hydrophobic inner core.[19] Considering the future application as thermosensitive drug delivery vehicles, such as responding to local hyperthermia, it was highly desirable that the T_{cp} of the thermosensitive PIC micelles should be constant regardless of the wide concentration range under physiological conditions. Moreover, the present PIC micelles might be dissociated into free block ionomers not showing thermosensitivity under specific conditions, suggesting their facile separation after fulfilling their mission as a thermosensitive vehicle.

Conclusions

The controlled synthesis of oppositely charged block ionomers (P*i*PrOx-P(Lys) and P*i*PrOx-P(Asp)) was achieved via ring-opening anionic polymerization of *N*-carboxyanhydrides (NCA) (ε-benzyloxycarbonyl-L-lysine (Lys(Z)-NCA) and β-benzyl-L-aspartate (BLA-NCA)) with ω-amino-functionalized P*i*PrOx macroinitiators and the subsequent deprotection reaction. Then, polyion complex (PIC) micelles were prepared by the complexation of P*i*PrOx-P(Lys) and P*i*PrOx-P(Asp) under physiological conditions. It was confirmed that the PIC micelles were spherical particles with small polydispersity indices and were very stable without any secondary aggregates. Furthermore, these PIC micelles had a constant phase-separation temperature (ca. 32 °C) under physiological conditions regardless of the wide ranges of concentration, reflecting the increased local concentration of the P*i*PrOx segments in the shell layer. In this respect, the P*i*PrOx-based PIC micelles might have promising applications, especially as a thermosensitive drug carrier loading charged biomacromolecules that include proteins, nucleic acids, and enzymes.

Acknowledgment. This work was financially supported by Special Coordination Funds for Science and Technology from the Ministry of Education, Culture, Sports, Science and Technology of Japan (MEXT) and by the Core Research for Evolution of Science and Technology (CREST), Japan Science and Technology Corporation (JST). We express our appreciation to Professor Woo-Dong Jang, The University of Tokyo (Present address: Yonsei University, Korea) and Mr. Shigeto Fukushima, Nippon Kayaku Co., Ltd., Japan, for their help with the NCA synthesis and Ph.D. candidate Michiaki Kumagai, The University of Tokyo, for his support with the acquisition of the TEM image.

Supporting Information Available: MALDI-TOF mass spectrum of Me-P*i*PrOx-acrylate obtained after the conversion reaction. ^{1}H NMR spectra of Me-P*i*PrOx-acrylate in D_2O, Me-P*i*PrOx-PBLA in DMSO-d_6, and P*i*PrOx-P(Asp) in D_2O. Gel permeation chromatograms of Me-P*i*PrOx-NH_2 and Me-P*i*PrOx-PBLA. Transmittance changes for 45C52/45A53 in the absence and presence of NaCl. This material is available free of charge via the Internet at http://pubs.acs.org.

LA061431J

(19) Nakayama, M.; Okano, T. *Biomacromolecules* **2005**, *6*, 2320.

シンポジウム「運動器の10年」変形性関節症の病態解明・診断・治療の新世紀

MRIを用いた変形性膝関節症の客観的な重症度評価指数の確立*

佐粧孝久[†]　中川晃一[†]　鈴木昌彦[†]　田原正道[†]　落合信靖[†]
荻野修平[†]　守屋秀繁[†]　和田佑一[‡]　中口俊哉[§]　三宅洋一[§]

緒　言

変形性膝関節症(osteoarthritis, OA)の重症度を客観的に評価することは，症例に応じた治療法の適切な選択を可能とし，治療体系を形成する上で有用となるものである．また，それの経時的な評価は，疾患の進行速度や各種治療法の効果判定を可能とする．

X線によるOAの評価は客観的な指標の1つと考えられている．実際にX線のグレードと疾患の重症度は関連があるとの報告がある[1),2)]．しかしその一方で，関連がないという報告もある[3),4)]．われわれも日常診療上，しばしば画像所見と臨床像との間に解離があることを経験する．したがって，X線検査はOAの診断に必要なものであり，重症度を把握する補助となるが，これのみに依存して重症度を決めることはできない．その他に，疾患の重症度を示す指標としてバイオマーカーも検討されている[5)]．しかし，確立したものとはなっていない．また，バイオマーカーの場合，他の関節の状態にも左右されるものである．よって，ある特定の関節の状態を把握するという意味においてはX線検査以外の画像検査が必要とされる．そこでわれわれはMRI(magnetic resonance imaging)所見に着目した．すなわち，内側型OAにおいて，進行するに従い明らかとなってくる大腿骨内側顆(medial femoral condyle, MFC)の輪郭の不整像に着目したのである(図1)．そこでプレリミナリーな検討として，他の目的に開発されたソフトウェアを用いて，不整度を数値化し膝機能スコアとの相関を調べた．その結果，不整度と膝機能の間に負の相関があることがわかった．すなわち不整度が大きくなると膝機能が低下するということがわかり，不整度の計測が客観的なOAの重症度の指標となる可能性を示した[6)]．われわれはこの結果を元に新しいソフトウェアを開発し，不整度測定の再現性と精度を高めた．本稿ではこの新しいソフトウェアが客観的なOAの重症度の指標となりえるかを検討した．さらに，人工膝関節置換術(total knee arthroplasty, TKA)施行時に得られた試料に免疫組織学的検討を加え，MRIで見られた不整像の意義につき検討を加えた．

Key words: Osteoarthritis, MRI, Subchondral bone, Severity, X-ray grading

*Objective Assessment of Severity of Osteoarthritic Knee Using MRI

[†]千葉大学大学院医学研究院整形外科学．Takahisa Sasho, Koichi Nakagawa, Masahiko Suzuki, Masamichi Tahara, Nobuyasu Ochiai, Shuhei Ogino, Hideshige Moriya: Department of Orthopedic Surgery, Graduate School of Medicine, Chiba University
[‡]帝京大学医学部整形外科学教室．Yuichi Wada: Department of Orthopaedic Surgery, Teikyo University School of Medicine
[§]千葉大学工学部．Toshiya Nakaguchi, Yoichi Miyake: Department of Engineering, Chiba University

対象と方法

1. 対象と膝機能評価

対象は内側型OA56膝である．男性が17名，女性が39名，平均年齢が73歳(50-73歳)であった．23膝はのちにTKAを受け，23膝はのちに鏡視下手術を受けることとなったが，本検討を施行した時点では外科的な治療を受けた例はなかった．全例，MRI撮像時の膝機能の評価をJOAスコアとLysholmスコアにて施行した．

2. ソフトウェア

MRI撮像に使用したのはシグナ1.5テスラ(GE medical system)である．プロトン密度強調の矢状断像を検討に用いた．撮像に用いたパラメータは2000/16 ms (TR/TE)，FOV14 cm×14 cm，matrix number 512×512，number of excitation 2，slice thickness

日整会誌 (J. Jpn. Orthop. Assoc.) 81 (1) 2007

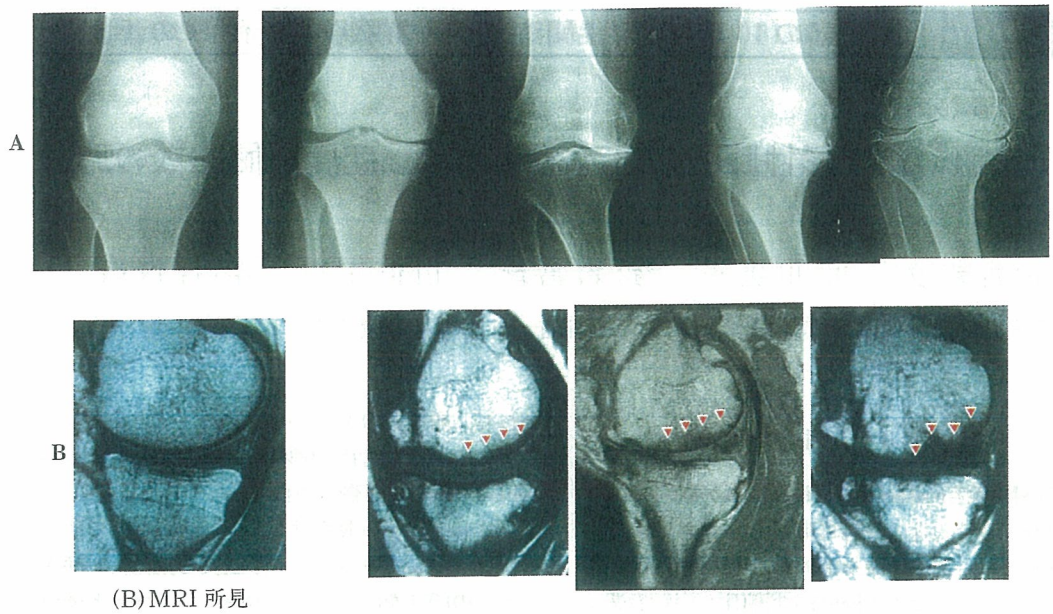

図1 進行した OA の MRI で見られる軟骨下骨領域の変化．上段(A：X 線所見)は右に行くに従い X 線グレードが上がっている．これに応じて，下段(B：MRI 所見)においても，右に行くに従い X 線グレードの高い症例の内側コンパートメントの矢状断像を示しているが，矢頭で示すように大腿骨内側顆の輪郭に不整な像が出現してくることがわかる．

3 mm, slice gap 0 mm である．各症例につき内側コンパートメントの中央に相当する 2 スライスを測定に使用し，平均値をその膝の値とした．統計学的検討には Pearson の相関係数，または Mann-Whitney's U test を用いた．

新しく開発したソフトウェアの特徴であるが，① Matlab 6.5 を用いてプログラミングしたソフトであること，② MRI の DICOM データを直接使用し計測が可能であること，③計測が半自動的に行えるようになっていること，などである．②の特徴により，プレリミナリーな検討の際に問題点の 1 つであった，1 度フィルムとなった画像をもう 1 度スキャンしてコンピュータに取り込むという操作がなくなった．

ここで不整度の計測法を紹介する．まず，MRI の DICOM データをコンピュータに取り込み，コンピュータ上で計測すべきスライスを選択する(図 2-A)．ついで画像を構成するピクセルの濃淡のヒストグラムを元に白黒画像化する(図 2-B)．その後に MFC の輪郭を抽出するが，この過程では自動的に輪郭の上縁と下縁が青と赤でトレースされる(図 2-C)．

不整度に関係するパラメータとして計測されるのは上縁と下縁で囲まれた面積(Area)，上縁の長さと下縁の長さの比，つまり青い線の長さを赤い線の長さで割ったもの(Ratio)，上縁と下縁の間の距離をピクセルごとに計測し 2 乗したものの和(Error)の 3 つの数値である(図 3)．

3. 免疫組織学的検討

組織学的な検討である．TKA 施行時の大腿骨遠位骨切除時に得られる MFC，大腿骨外側顆(lateral femoral condyle, LFC)を試料とした．得られた試料は 4%パラフォルムアルデヒドで 48 時間固定後，20% EDTA で脱灰し，組織標本を作製した．試料は HE (hematoxyline-eosin)染色に加え，疼痛関連物質である Cox-1,Cox-2,TNF-α(tumor necrosis factor-2)，また神経線維の存在を調べるために TUJ1 で染色した．TUJ1 はラットの脳から得られた微小管に対する抗体として作成されたもので，神経特異的なクラスIII-ベータチュブリンを認識する[7]．

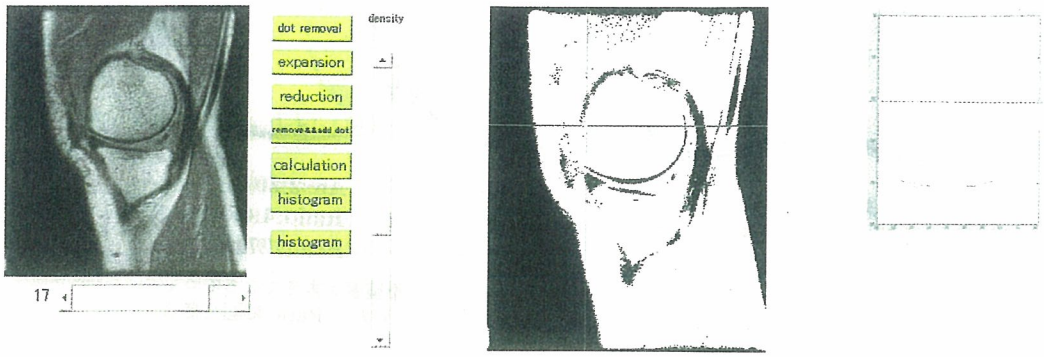

図2　大腿骨内側顆(MFC)の輪郭の抽出．MRI の DICOM データをコンピュータに取り込み，コンピュータ上で計測すべきスライスを選択する(A)．ついで画像を構成するピクセルの濃淡のヒストグラムを元に白黒画像化する(B)．その後に MFC の輪郭を抽出するが，この過程では自動的に輪郭の上縁と下縁が青と赤でトレースされる(C)．

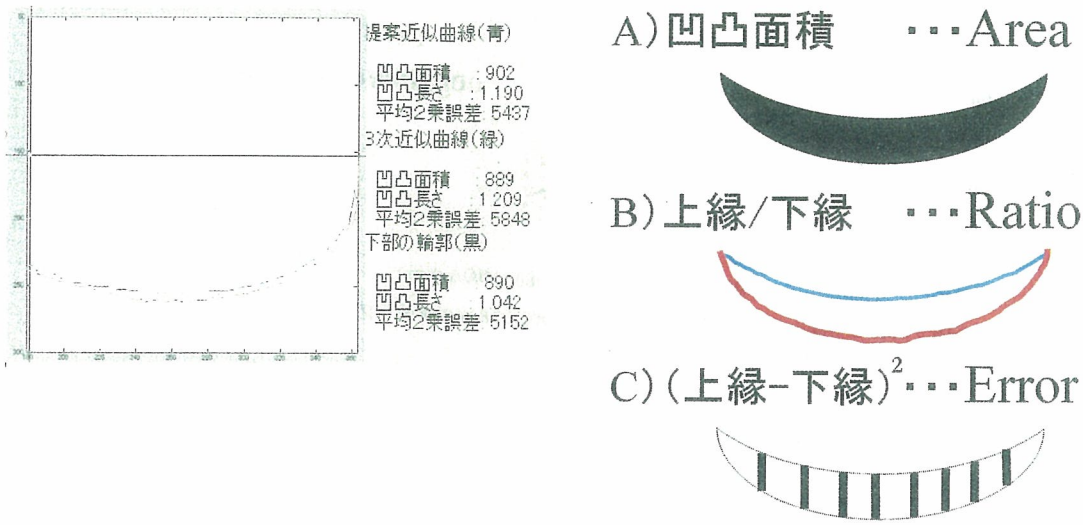

図3　計測されるパラメータ．不整度に関係するパラメータとして計測されるのは上縁と下縁で囲まれる部位の面積：Area，上縁の線の長さと下縁の線の長さの比：Ratio，ピクセルごとに計測された幅の2乗の和：Error の3つの数値である．

結　　果

1. 不整度の計測と膝スコア

計測した3つの値と抽出した輪郭の関係を，代表的な例を用いて示した(図4)．4つの輪郭のうち右に行くほど肉眼的には不整が強いように見える．したがって各パラメータも右に行くに従い上昇する．しかし，Ratio においては症例3のほうが症例4より大きな値となっている．3つのパラメータは互いに独立したものではないと考えられるが，症例によってはこのように値が逆転することもある．

不整度を表す3つのパラメータと膝スコアの関係であるが，代表的な例として JOA スコアと Area の関係をグラフに示した(図5)．相関係数−0.489 で負の相関を認める．すなわち，不整度が大きくなると膝機能が低下することを表している．JOA スコアのうち，疼痛に関連する歩行時の痛み，階段昇降時の痛みと Area の関係を調べると歩行時の痛みと Area がよく相関することがわかった(図5)．Lysholm スコアと Area も相関係数が−0.381 と負の相関を認めた．他の2つのパラメー

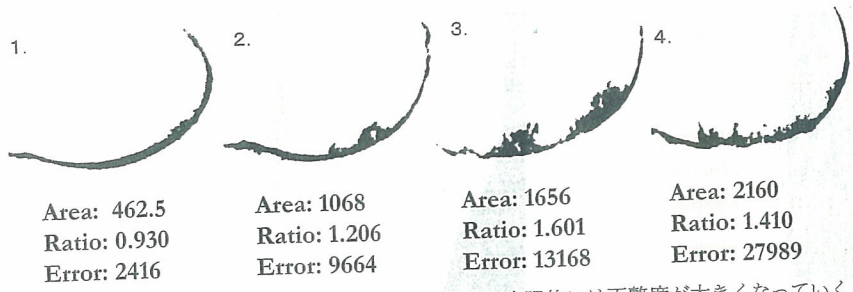

図4 代表例の計測値．症例1から4に進むに従い，肉眼的には不整度が大きくなっていくが，各例に対応した3つの計測値も右に行くに従い大きくなる．ただしRatioに関しては3と4の間で逆転が起こっている．

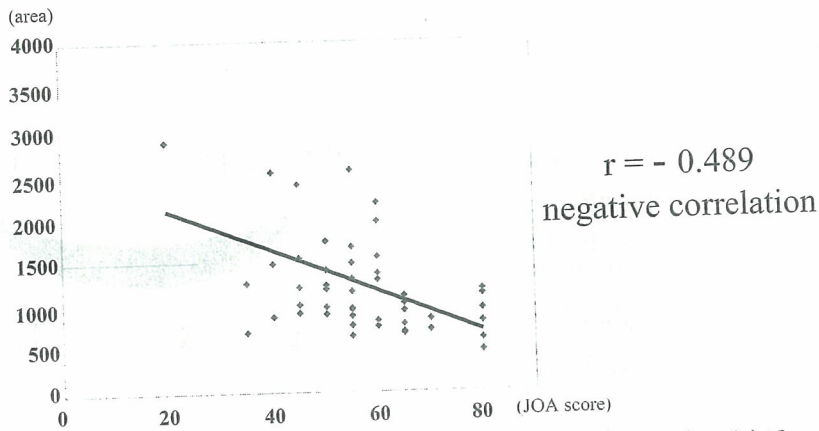

図5 JOA scoreとAreaの関係．JOA scoreとAreaをグラフにプロットしてみると，負の相関のあることがわかった．

表1 3つのパラメータと膝機能スコアの関係

	Area	Ratio	Error
JOAスコア	−0.489*	−0.533*	−0.448*
歩行時の疼痛	−0.361*	−0.468*	−0.414*
階段昇降時の疼痛	−0.148	−0.200	−0.103
Lysholmスコア	−0.381*	−0.441*	−0.380*

3つのパラメータとJOAスコアの総点数，JOAスコアの内訳として歩行時の疼痛，Lysholmスコアの総点数と負の相関があった．JOAスコアの内訳として階段昇降時の疼痛とは相関がなかった．*Statistically significant

タであるRatio，ErrorともにAreaと同様の傾向を示し，JOAスコアの総点数，内訳として歩行時の疼痛，Lysholmスコアの総点数と負の相関があった(表1)．

2. 免疫組織学的検討

HE染色ではMFCの軟骨下骨の骨梁の乱れや軟骨下骨にpseudocystの形成が見られた．強拡大では同部は，軟骨下骨や石灰板に接して存在する線維性組織であった(図6)．この組織はShibakawaらがbone resorption pitと名づけた骨髄由来の組織であると考えられる[8]．MFCに形成されたこの線維性組織内にはCox-2陽性細胞が存在することがわかった(図7-A)．しかし

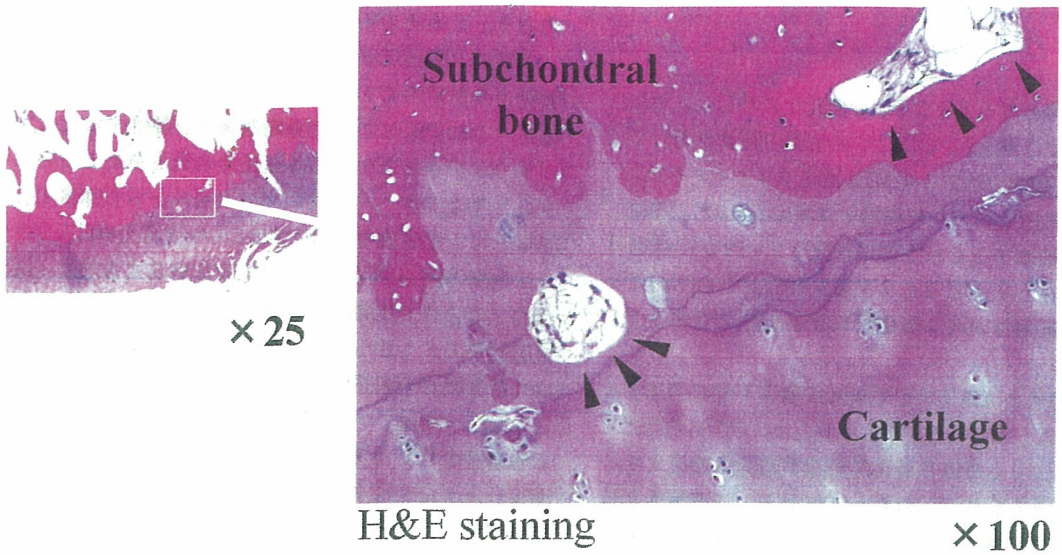

図6 軟骨下骨領域の病理像．MFC の軟骨下骨の骨梁の乱れや軟骨下骨に矢頭で示すように pseudocyst の形成が見られた．拡大すると pseudocyst のように見えるのは，軟骨下骨や石灰板に接して存在する線維性組織の形成であった．(HE 染色)

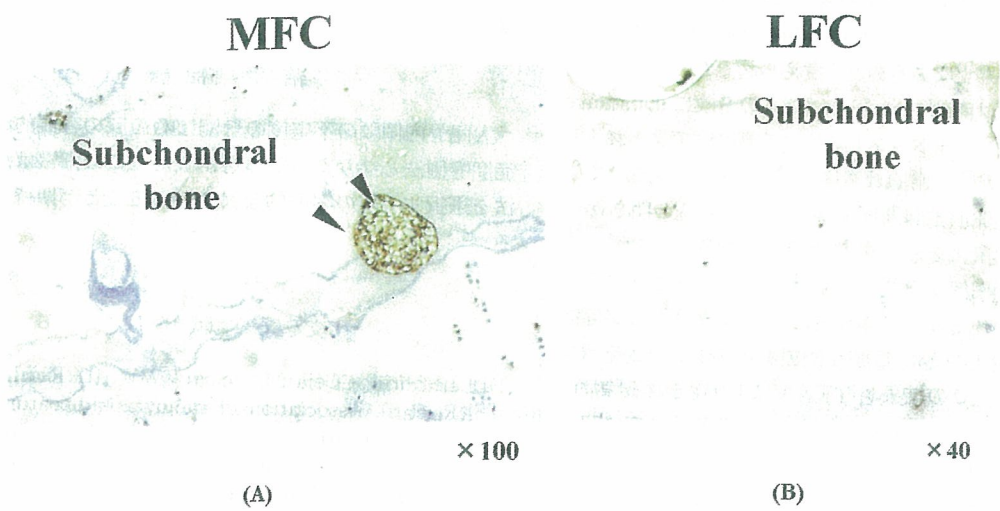

図7 軟骨下骨領域の免疫染色(COX-2)．MFC に形成されたこの線維性組織内には Cox-2 陽性細胞が存在することがわかった(A)．しかし LFC には Cox-2 陽性細胞は存在しなかった(B)．

LFC には Cox-2 陽性細胞は存在しなかった(図 7-B)．また，同部位は TNF-α 陽性の細胞が存在することもわかった(data not shown)．さらには TUJ1 陽性の細胞も存在した(data not shown)．免疫染色の結果をまとめると MFC では調べた 20 例のうち Cox-1 陽性の症例が 30%，Cox-2 陽性例が 100%，TNF-α 陽性例が 90%，TUJ1 は 15 症例の検討であるが，100%陽性であった．一方，LFC ではいずれの抗原も陰性であった．

考　　察

図1に見られるようなMFCの変化に着目し，われわれは今までにMRI上のMFCの輪郭の評価を施行してきた[6),9)]．初期の方法ではMRI画像をスキャナーでコンピュータに取り込み，白黒画像に変換したのち，MFCの輪郭を抽出するという方法を取っていたが，今回は新たなソフトウェアにより不整度計測が半自動的になり，より再現性が高く客観的に数値が算出できるようになった．

MRIで見られるMFCの輪郭は軟骨下骨に相当すると考えられる．つまりMFCの不整とは，OAの進行に伴い出現してくる軟骨下骨の組織学的変化を捉えているものと考えられる．われわれが示した，不整度と膝スコアが負の相関を示したということは軟骨下骨の組織学的変化がOAの重症度の指標となりえることを示したものである．特に，疼痛関連物質であるCox-2やTNF-αが高率に陽性であることは，軟骨下骨に起きる組織学的変化はOAの膝の疼痛に強く関係していることが示唆される．これまでOAの膝の疼痛は滑膜炎[10)]や骨髄圧の上昇[11)]によるものと考えられてきた．また，内側型OAでは内側コンパートメントの滑膜にsubstance Pが外側コンパートメントに比べて高頻度で見られるとの報告もあり[12)]，滑膜は疼痛を感知する場ともなっている．一方，変形性膝関節症が進行してくると明らかな組織学的な変化を起こす軟骨下骨は疼痛発生の場，または疼痛を感知する場としてはあまり考慮されることがなかった．しかし，本検討の結果は軟骨下骨が疼痛発生の場の1つとして重要な位置を占めることを示すものである．この結果からTKAにより得られる除痛のメカニズムとして，TKA施行時には必然的に病的変化を生じた軟骨下骨の切除が行われており，これにより除痛が達成されているのではないかと考えている．つまり，軟骨下骨のデブリドマン効果であると考えている．

MRI上の不整度測定の臨床的意義であるが，今後不整度に応じた適切な治療法を検討することで，治療法を選択する際の指標となることが期待できる．ただし，本研究の対象となった症例の多くは手術療法を必要としており，進行例が多かった．より軽症例では軟骨下骨の変化はあまりないと考えられること，また軽症例では多くの場合，半月板の変性断裂による症状も疼痛に関与することが考えられることから，軟骨下骨を評価する本方法は，進行例した例にのみ適応可能な方法であろうとは考えている．

本研究の問題点は3つ挙げられる．第1点目は大腿骨側のみを評価しており，脛骨側を見ていないことである．これに関しては大腿骨内側顆を評価することでミラーリジョンとなっている脛骨の変化を捉えているものと考えており，内側コンパートメントを代表する指標として大腿骨内側顆はふさわしいと考えられる．さらに大腿骨顆部は膝蓋骨とも関節を形成するため，進行例では膝蓋大腿関節へと進展したOAも捉えている可能性がある．しかし，将来的には脛骨や膝蓋骨をも含めた評価法が理想的であるとも考えている．第2点目として，内側コンパートメントの矢状断2スライスでのみ評価していることがあげられるが，MRIがより進歩し，またそれに対応したよりよいソフトウェアを開発することで三次元的に評価することが将来的には必要になると考えている．第3点目は，明らかなX線所見があるが症状に乏しい症例での検討がなされていないことである．つまりネガティブコントロールに相当する症例での検討がなされていないことが，今後の課題と言える．

結　　語

大腿骨内側顆の不整度の計測はOA膝の客観的な重症度評価法となりえることを示した．この指標は治療法を選択する際の客観的な目安となることが期待できる．

文　　献

1) Lethbridge-Cejku M, Scott WW Jr, Reichle R, et al. Association of radiographic features of osteoarthritis of the knee with knee pain: data from the Baltimore Longitudinal Study of Aging. Arthritis Care Res 1995; 8: 182-8.
2) Hopman-Rock M, Odding E, Hofman A, et al. Physical and psychosocial disability in elderly subjects in relation to pain in the hip and/or knee. J Rheumatol. 1996; 23: 1037-44.
3) Hannan MT, Felson DT, Pincus T. Analysis of the discordance between radiographic changes and knee pain in osteoarthritis of the knee. J Rheumatol 2000; 27: 1513-7.
4) Meding JB, Ritter MA, Faris PM, et al. Does the preoperative radiographic degree of osteoarthritis correlate to the results in primary total knee arthroplasty? J Arthroplasty 2001; 16: 13-6.
5) Bruyere O, Collette J, Kothari M, et al.